

## REPORT DOCUMENTATION PAGE

Form Approved  
OMB No. 0704-0188

Public reporting burden for this collection of information is estimated to average 1 hour per response, including the time for reviewing instructions, searching existing data sources, gathering and maintaining the data needed, and completing and reviewing the collection of information. Send comments regarding this burden estimate or any other aspect of this collection of information, including suggestions for reducing this burden, to Washington Headquarters Services, Directorate for Information Operations and Reports, 1215 Jefferson Davis Highway, Suite 1204, Arlington, VA 22202-4302, and to the Office of Management and Budget, Paperwork Reduction Project (0704-0188), Washington, DC 20503.

1. AGENCY USE ONLY (Leave blank)	2. REPORT DATE	3. REPORT TYPE AND DATES COVERED	
	18 Feb 1997	Final 1 July 92 - 30 Sep 96	
4. TITLE AND SUBTITLE <b>Elastic and Anelastic Structure Beneath Eurasia</b>			5. FUNDING NUMBERS PE 61102F Proj 2309/AS F49620-92-J-0392
6. AUTHOR(S) Goran Ekstrom Adam Dziewonski Gideon Smith & Wei-jia Su			
7. PERFORMING ORGANIZATION NAME(S) AND ADDRESS(ES) Dept of Earth and Planetary Sciences Harvard University Cambridge MA 02138			8. PERFORMING ORGANIZATION REPORT NUMBER Not numbered
9 SPONSORING MONITORING AGENCY NAME(S) AND ADDRESS(ES) AFOSR/NM 110 Duncan Ave Bolling AFB DC 20332			10. SPONSORING / MONITORING AGENCY REPORT NUMBER Monograph Series of Seismic Research #97-03
11. SUPPLEMENTARY NOTES			
12a. DISTRIBUTION AVAILABILITY STATEMENT APPROVED FOR PUBLIC RELEASE: DISTRIBUTION UNLIMITED		12b. DISTRIBUTION CODE	
13 ABSTRACT (Maximum 200 words) The primary objective of this work has been to map the variations of elastic mantle properties beneath Eurasia over horizontal length scales of approximately 1000-1500 kilometers and vertical length scales of 50-100 kilometers in the upper mantle. Large and diverse datasets of seismic waveforms, absolute and relative body wave travel times, and surface wave phase velocity and amplitudes have been collected and have been analyzed. Several tens of thousands of measurements of intermediate period surface wave dispersion have been made in order to characterize and properly account for the highly heterogeneous velocity structure associated with the crust and the uppermost mantle. Global maps of phase velocity for Love and Rayleigh waves in the period range 35-150 seconds have been produced. The new dataset of surface wave dispersion has been combined with previously collected data in the finalization of a new 3-D whole mantle model. In comparison with previous Harvard mantle models the horizontal resolution has been increased by expanding the global structure up to spherical harmonic degree $l = 20$ , and a radial parameterization has been adopted which gives better vertical resolution in the upper mantle.			
14. SUBJECT TERMS Seismology Earth elastic properties Velocity model			15. NUMBER OF PAGES 51
			16. PRICE CODE
17. SECURITY CLASSIFICATION OF REPORT UNCLASSIFIED	18. SECURITY CLASSIFICATION OF THIS PAGE UNCLASSIFIED	19. SECURITY CLASSIFICATION OF ABSTRACT UNCLASSIFIED	20. LIMITATION OF ABSTRACT SAR

## Final Report

### Elastic and Anelastic Structure Beneath Eurasia

Göran Ekström (P.I.), Adam M. Dziewonski, Gideon P. Smith and Wei-jia Su

Department of Earth and Planetary Sciences  
Harvard University  
Cambridge, MA 02138

Contract No. F49620-92-J-0392  
Sponsored by AFOSR

#### Abstract

We have collected and analyzed large and diverse datasets of seismic waveforms, absolute and relative body wave travel times, and surface wave phase velocities and amplitudes. Our primary objective has been to map the variations of elastic mantle properties beneath Eurasia over horizontal lengthscales of approximately 1000–1500 km and vertical lengthscales of 50–100 km in the upper mantle.

In order to characterize and properly account for the highly heterogeneous velocity structure associated with the crust and uppermost mantle, we have made several tens of thousands of measurements of intermediate period surface wave dispersion, and have developed global maps of phase velocity for Love and Rayleigh waves in the period range 35–150 s. The new maps, expanded in spherical harmonics up to degree 40, provide up to 96% reduction of the variance observed in the phase measurements, and, at short periods, show a very strong correlation with the thickness of the crust and the surface geology. The new dataset of surface wave dispersion, which provides excellent constraints on crustal and lithospheric structure, has been combined with previously collected data in the finalization of our new 3-D whole mantle model. In comparison with previous Harvard mantle models, such as S12WM13, we have increased the horizontal resolution by expanding the global structure up to spherical harmonic degree  $l = 20$ , and we have adopted a radial parameterization which gives better vertical resolution in the upper mantle.

The new model shows many of the same features seen in previous tomographic images, but with significantly sharper definition, in particular in the upper mantle. Lithospheric roots beneath the stable continental interiors are the most prominent feature in the uppermost mantle. A surprising and complicating result of our study is that when P/SV- and SH-sensitive data are inverted separately, differences in the resulting models are apparent in the middle of the upper mantle (200–300 km). The suggestion is that anisotropy may be a significant contributor to lateral heterogeneity, particularly beneath the oceans.

We have made efforts to validate our models, and to explore their utility in event location, through the prediction of  $Pn$  travel times. In some regions we obtain relatively good agreement between the observed residual and the  $Pn$  travel time predicted from the  $P$  and  $S$  model S&P12WM13 (expanded only to  $l=12$ ). In other regions the agreement is poor, probably indicating limited resolution of the structure in the uppermost mantle.

## Objective

We adapt the seismic tomographic techniques developed in global scale studies to the regional scale problem of mapping the elastic and anelastic material properties beneath Eurasia. The main objective of this research is to obtain a tomographic seismic velocity model for the structure beneath Eurasia with a horizontal resolution corresponding to at least  $l = 20$ , consistent with the widest possible range of seismological observations.

Use of tomographic models of the mantle in the calculation of teleseismic travel times have been shown to result in improved teleseismic event locations (*Smith and Ekström, 1996*). These models are therefore relevant to the global monitoring of a Comprehensive Test Ban Treaty, in particular for obtaining better locations for events in previously uncalibrated regions. In addition, the improved ability to model dispersed intermediate-period surface waves makes it possible to perform more efficient filtering and stacking and, as a consequence, to achieve both a lower surface wave detection threshold, and to obtain better surface wave magnitudes. The advance in our ability to model surface waves can therefore benefit both the detection and discrimination tasks of a monitoring program.

## Research Accomplished

In earlier reports (1993, 1994, 1995) we have presented preliminary results of our higher resolution upper mantle model S20U7L5. We have also shown the improvement of teleseismic event locations using heterogeneous mantle models. In this report we discuss (1) some results for the surface wave dispersion characterization at intermediate periods; (2) new indications for anisotropy in the upper mantle which have become apparent as we finalize the model S20U7L5, and; (3) modeling of  $Pn$  residuals using global tomographic models. An extensive report on the surface wave dispersion results (1), in the form of a preprint, is included as an appendix.

### *Surface Wave Dispersion*

Due to their sensitivity to the elastic structure of the crust and the top of the mantle, measurements of intermediate-period surface wave dispersion are ideal for imaging the shallowest portions of the Earth. The main difficulty in obtaining dispersion measurements from telesismically observed surface waves at periods less than about 100 s is that variations in phase velocities are sufficiently big to cause path variations of several cycles in phase, and isolated residual phase measurements  $[-\pi, \pi]$  at a single period are therefore ambiguous in multiples of  $2\pi$ . For minor arc observations, phase measurements at periods longer than 100 s can, however, be associated with a total cycle count. If a continuous dispersion curve can be anchored at long periods, the total phase perturbation can then be inferred without ambiguity.

In order to obtain the complete broadband dispersion, we have developed a method we call *iterative frequency band expansion*. We initially determine the dispersion parameters in a narrow frequency range centered around 100 s, and then, in several iterations, increase the higher frequency end of the total frequency range. In each iteration, the dispersion parameters are adjusted to minimize the residual dispersion between an observed and a model surface wave using the downhill simplex method of *Nelder and Mead (1965)*. Once a misfit between the two wavygroups is minimized for a given frequency range, the range is expanded to include higher frequencies. Because of the smoothness of the dispersion curve, a prediction can be made for frequencies slightly higher than the ones included in the previous iteration. This ensures that the phase difference between model seismogram and observed

seismogram always remains small, so that gradient methods continue to work in the next iteration.

This method of analysis has been systematically applied to digital seismograms from the IRIS/USGS, IRIS/IDA, GEOSCOPE, CDSN, GTSN, and MEDNET networks, using earthquake sources for the period January 1989–September 1995. Analysis was attempted for all earthquakes during this time period with  $M_w \geq 5.5$ . We use the moment tensors and centroid locations in the Harvard CMT catalog to calculate the source excitation. Only shallow earthquakes ( $h < 50$  km) were included, in order to maximize the excitation of surface waves. In addition, we only consider paths in the distance range  $25^\circ \leq \Delta \leq 150^\circ$ , in order to avoid problems of separation of the fundamental mode at short distances and close to the antipode.

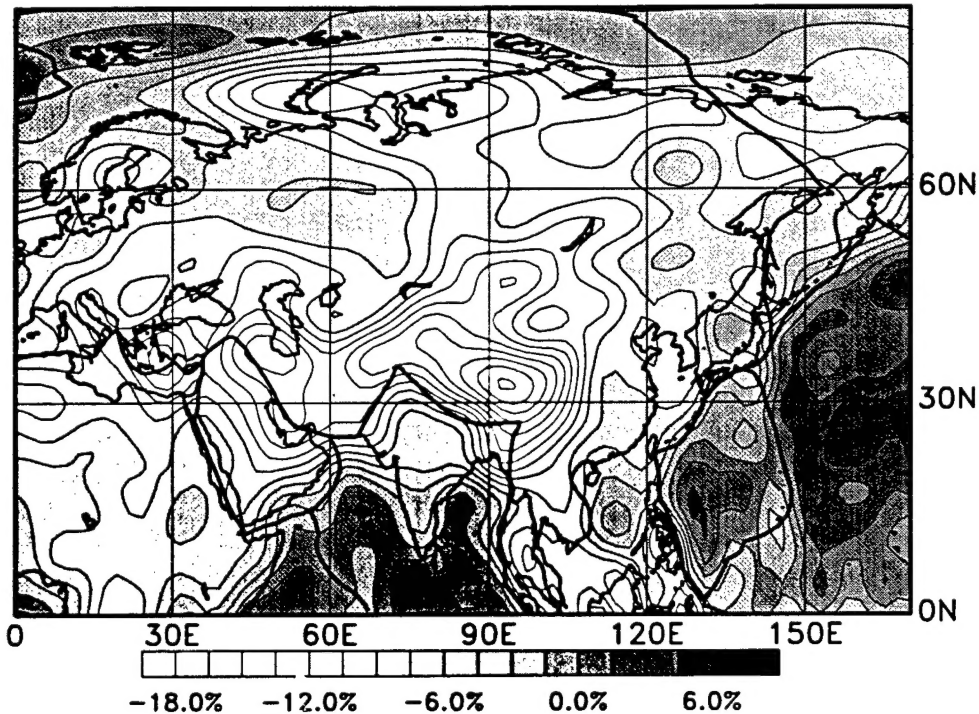


Figure 1: Map shows the phase velocity variations of 35 s Love waves for Eurasia. Note the strong correlation between slow velocities and thick and low-velocity crust.

More than 128,000 station-receiver paths were analyzed. Approximately 37,000 high-quality measurements for Rayleigh waves at 50 s resulted from the analysis, while at 35 s, the number was somewhat smaller — 28,000. Fewer good measurements were obtained for Love waves, in part due to the higher noise levels on horizontal components. In the analysis of the measurements, the dispersion curves were converted to phase anomalies  $\delta\Phi$  at the discrete periods 150, 100, 75, 60, 50, 45, 40, 37, and 35 s. Observational uncertainties of the measurements were determined from statistical analysis of repeated measurements for similar paths.

The phase anomalies were next inverted for the model coefficients of global phase velocity maps expanded in spherical harmonics. The predicted phase anomaly between a source at

$(\theta_S, \phi_S)$  and a receiver at  $(\theta_R, \phi_R)$  is written in terms of real spherical harmonics

$$\delta\Phi = -\frac{\omega}{c_0} \int_{(\theta_S, \phi_S)}^{(\theta_R, \phi_R)} \sum_{l=0}^L \sum_{m=0}^{m=l} (A_{lm} \cos m\phi + B_{lm} \sin m\phi) p_l^m(\theta) ds, \quad (1)$$

where  $A_{lm}$ ,  $B_{lm}$  are the model coefficients,  $L$  is the maximum angular degree of the expansion, and  $p_l^m$  are the Legendre polynomials. The coefficients  $A_{lm}$ ,  $B_{lm}$  are determined by damped least-squares inversion. The result of these inversions are global phase velocity maps (*Ekström et al.*, 1997). The model coefficients can be obtained in electronic form via anonymous ftp to `saf.harvard.edu`, by retrieving the files in `pub/ETL-JGR-96`.

The resulting maps explain 80–96% of the variance in Love wave phase anomalies, and between 70–90% of the Rayleigh wave data. The lowest variance reduction is obtained for the longest periods. Figure 1 shows the phase velocity map for Eurasia and Love waves at 35 s period. Clearly, a very large portion of the signal is associated (as expected) with the contrast between oceanic and continental crust and lithosphere. Within Eurasia, very large variations are seen which reflect both the total thickness of the crust (as beneath western Tibet), tectonic activity (the Alpine-Himalayan belt in general) and very thick sedimentary basins (Arctic ocean shelf, southern Caspian sea). Resolution experiments indicate that these features are well resolved. It is interesting to note that when compared with phase velocity predictions from the recent global crustal model CRUST-5.0 (*Mooney et al.*, 1995), there are some areas which show very large similarities, and other areas (in particular sedimentary basins) which do not. The correlation between the observed phase velocity map and that predicted by *Mooney et al.*'s model is approximately 0.80 for Love waves at 35 s.

#### *A degree 20 model of the Mantle*

The surface wave data described above have been used in conjunction with previous seismological datasets to derive a higher resolution 3-D model of the Earth's mantle. Preliminary results have been presented at various meetings (*Ekström and Dziewonski*, 1994; 1995; *Dziewonski et al.*, 1996).

The parameterization and inversion approach are similar to those used for earlier Harvard mantle models, such as S12WM13 (*Su et al.*, 1993), with the following notable differences:

- We use a split parameterization for the mantle, and parameterize the radial variations in the upper mantle in terms of Chebyshev polynomials of degree 0–7. For the lower mantle we use Chebyshev polynomials of degree 0–5.
- The spherical harmonic expansion is extended from degree 12 to degree 20.
- The data are corrected for crustal structure using a new compilation of crustal thicknesses and velocities by *Mooney et al.* (1995). This is in contrast to previous models which were only corrected for average continental and oceanic crustal structure.

Several types of data with sensitivity to velocity variations in different parts of the mantle are included. The following data have been incorporated in the derivation of the new model

- Absolute and differential travel times measured from waveform data ( $S$ ,  $SS$ ,  $ScS$ ,  $SS-S$ ,  $ScS-S$ ,  $ScSScS-ScS$ ,  $S-SKS$ ,  $SKKS-SKS$ ).
- Long-period body and mantle waveforms from earthquakes recorded on the Global Seismic Network.

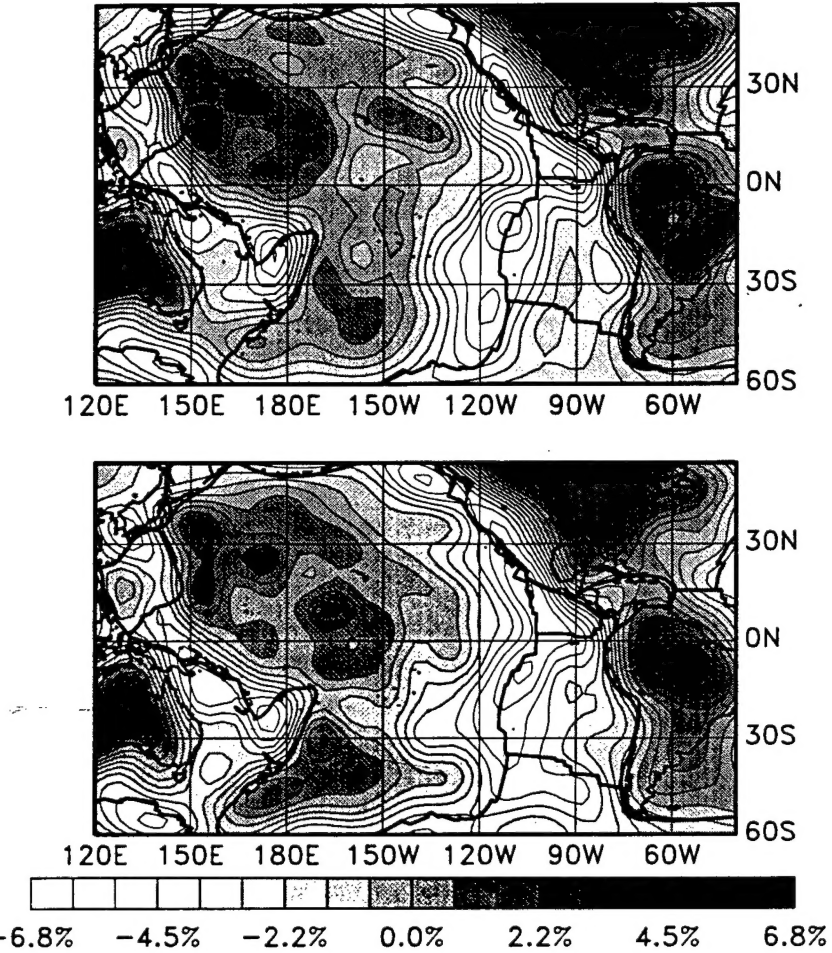


Figure 2: Maps show the  $S$  velocity variations at 100 km depth beneath the Pacific and adjacent areas. The top panel shows the  $S$ -velocity variations recovered from primarily P/SV-sensitive data, and the bottom panel for SH-sensitive data. There is strong similarity between the two maps in most regions.

- Very long-period mantle waveforms from large earthquakes recorded on the Global Seismic Network.
- Intermediate period dispersion measurements of Rayleigh and Love waves (described above).

The new model S20U7L5 shows many of the same features seen in previous tomographic images, but with significantly sharper definition. On a global scale, the fast velocities beneath stable continental interiors are the most prominent anomalies in the top 300 km of the mantle. The very high velocities beneath the stable interior of West Africa continue even deeper. The new model also shows that the slow velocity anomalies associated with ridges continue to great depth, in particular in the Indian Ocean. The Red Sea rift shows slow velocities extending down to 400 km. Below 250 km slow features not directly associated with surface tectonics predominate, in particular in the center of the Pacific Ocean.

In order to investigate the compatibility of the various datasets, we have performed several

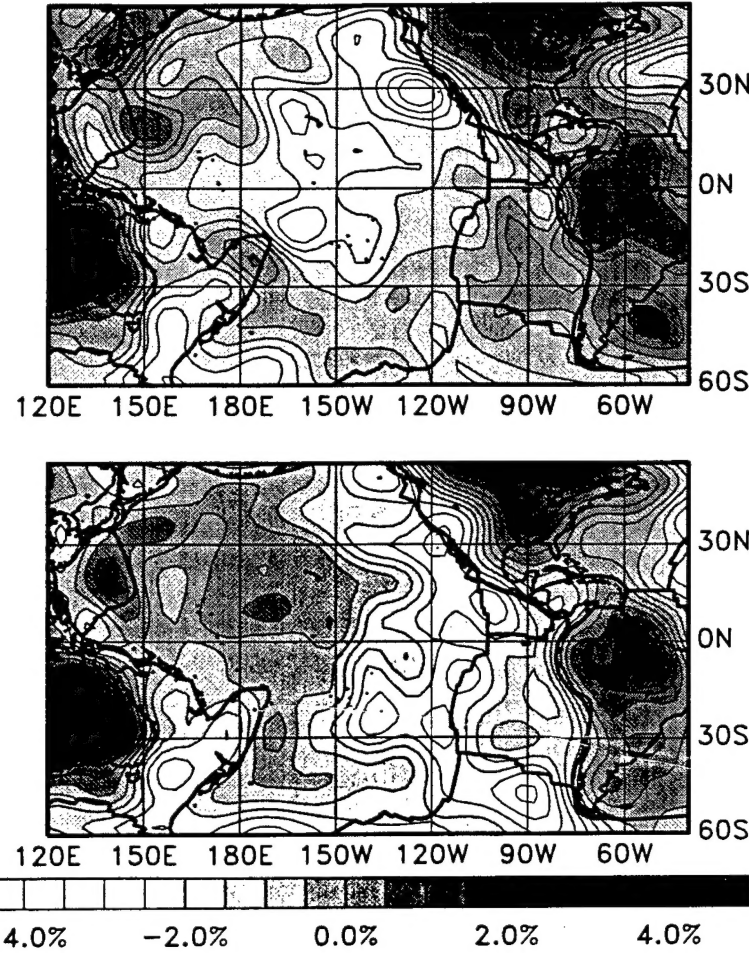


Figure 3: Maps show the  $S$  velocity variations at 200 km depth beneath the Pacific and adjacent areas obtained from separate inversions of P/SV and SH sensitive data. Note the slow velocities in the central Pacific seen in the top (P/SV) map, but absent in the bottom (SH) map. Also, the East Pacific Rise remains a slow feature at this depth for SH data, but not for P/SV data.

inversions using subsets of the full dataset. In particular, we have separated the data which are primarily sensitive to SH-type structure from those which primarily sense P/SV-type structure, by considering separately observations made from transversely polarized seismograms and those made on vertical and radial seismograms. The somewhat surprising result is that there are regions and depth ranges where we obtain distinctly different patterns in the separate inversions. In Figure 2 we show a comparison of the structures at 100 km depth beneath the Pacific as imaged using the two sets of data. While there are differences between the two maps, overall there is fairly close agreement. Mostly we see the fast roots beneath the continents, and the signature of the hot and cooling lithosphere in the oceans. At 200 km (Figure 3), however, the slow velocity in the central Pacific seen in the P/SV map (as well as in many previous models) is not seen in the SH map, which instead shows consistently fast velocities in the same region. The SH map also shows slower velocities at this depth associated with the East Pacific Rise, while the P/SV map does not.

There are different possible explanations for this result. The most straightforward reason could be that this is the effects of varying levels of transverse anisotropy in the asthenosphere. A second possibility is that azimuthal anisotropy in the oceanic lithosphere and/or asthenosphere gets mapped, through the ray coverage, into different apparent velocity structures for Love and Rayleigh waves. A third possibility is that we have overestimated the resolving power of the different datasets, and that the observed patterns are spurious. Based on the robustness of the results (established through additional experiments), we do not believe the third explanation is likely, and we are currently exploring the need for including specific considerations of anisotropy in future modeling efforts.

### *Modeling of Regional Phases*

The limited distribution of sources and the sparse (in a global sense) distribution of receivers set a limit on our ability to simply keep increasing the resolution of our global models. To obtain good global resolution on the scale of 500 km or less will probably be very difficult, if not impossible, for some time to come. It is possible though to obtain high resolution models of a number of regions, both large and small, that are well sampled. To obtain the best possible coverage in a given region, one would ideally use sources and receivers that are both within and outside the region of interest. Proper treatment of such a combination of data would require a hybrid parameterization (*Fukao et al.*, 1992).

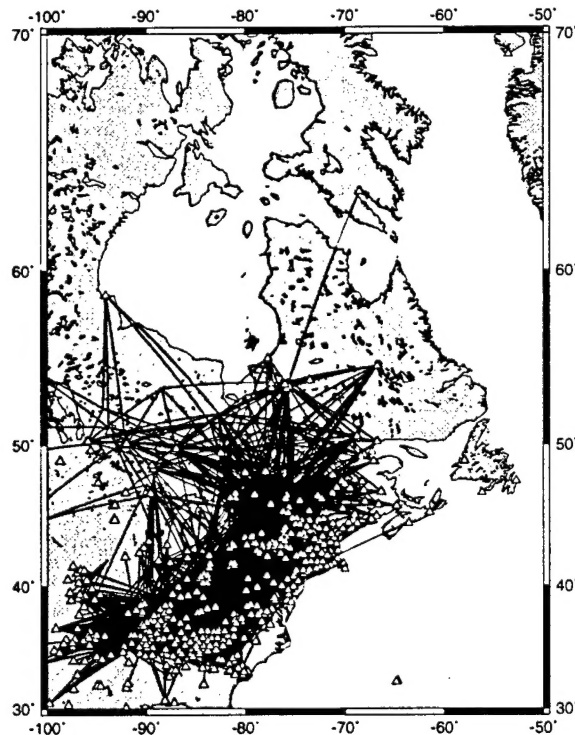


Figure 4: Map showing ray coverage for  $Pn$  observations in northeastern U.S., reported in the ISC.

In a preliminary investigation we have been examining how well our current 3-D mantle models may be used to explain trends in regional data in different regions. In Figure 4 we

show the  $Pn$  raypath coverage for events reported by the ISC for northeastern North America. This region was chosen to test our model in an area where we predict large anomalies based on the model S&P12WM13 (*Su and Dziewonski, 1993*) and have a good path coverage using data from the ISC.

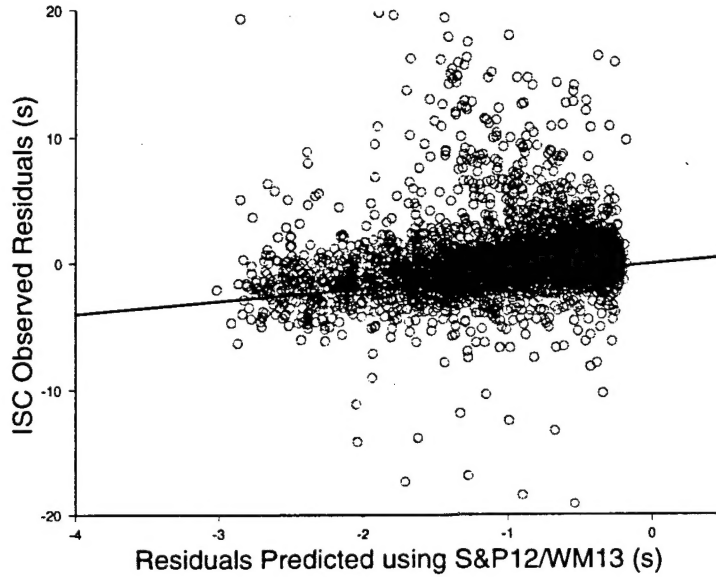


Figure 5: Observed residuals for  $Pn$  compared with predictions from S&P12WM13 for paths in northeastern U.S.

Figure 5 shows the observed and calculated  $Pn$  residuals for this region. The  $Pn$  travel time was calculated using the average  $P$  velocity at the top of the mantle in the model S&P12WM13. Despite some scatter a correlation between the residuals found for these regional phases and those derived from our global model can be seen. In particular, the level of heterogeneity appears to be well matched. A second region for which we performed this experiment was southern Eurasia. This region has many fewer stations reporting to the ISC. Figure 6 shows the ISC residuals and the predicted residuals. In this case there is no apparent correlation. This may be for one of several reasons: there is some evidence that earthquakes in this region are poorly located; our model in this region may not be so well constrained due to lack of data coverage; structure in this region may be more complex than the resolution of our current model allows; or the correlation may be obscured due to the smaller range of predicted anomalies.

Despite being based wholly on teleseismic data, our current global models appear to provide fairly good estimates of uppermost mantle velocities beneath regions such as northeastern North America. The experiment also suggests that beneath areas such as Eurasia regional phases may need to be included to adequately model the uppermost mantle structure. However, such an analysis will require careful relocation of the seismicity before utilizing the travel times. With the inclusion of regional data, parameterization in terms of spherical harmonics is a poor choice since by definition they have a uniform resolution everywhere. In future work, we will instead move towards hybrid parameterizations with variable resolution, to be able to include and subsequently to better model observations corresponding to both regional and teleseismic distances.

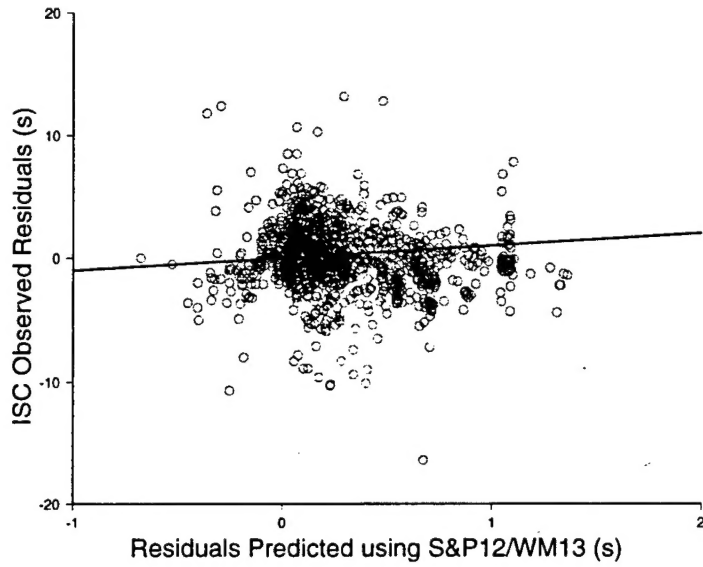


Figure 6: Observed residuals for  $Pn$  compared with predictions from S&P12WM13 for paths in southern Eurasia.

## Conclusions and Recommendations

By combining a large number of diverse seismological observations, we have made progress towards obtaining higher resolution tomographic images of the regional scale elastic structure globally and beneath Eurasia. The shallowest part of the mantle is effectively constrained and imaged using intermediate period surface waves. Both global and regional scale heterogeneity in the mantle has been shown to bias seismically derived event locations. In some regions, our current tomographic models can predict the gross residual patterns seen in regional phase data. It appears likely that further improvements in locations can be achieved by correcting for better known elastic heterogeneity in the Earth's mantle.

## References

Dziewonski, A. M., G. Ekström, and X.-F. Liu, Structure and the top and the bottom of the mantle, in *Proceedings of NATO Advanced Study Institute "Monitoring a Comprehensive Test Ban Treaty"* Alvor, Portugal, Jan., 1995, 521–550, 1996.

Ekström, G., and A. M. Dziewonski, Higher resolution upper mantle S velocity structure (abstract), 75, *EOS, Trans. Am. Geophys. Soc.*, 475, 1994.

Ekström, G., and A. M. Dziewonski, Improved models of upper mantle S velocity structure (abstract), 76, *EOS, Trans. Am. Geophys. Soc.*, 421, 1995.

Ekström, G., J. Tromp, and E. W. Larson, Measurements and global models of surface wave propagation, *J. Geophys. Res.*, in press, 1997.

Fukao, Y., M. Obayashi, H. Inoue, and M. Nenbai, Subducting slabs in the mantle transition zone, *J. Geophys. Res.*, 97, 4809–4822, 1992.

Mooney, W. D., G. Laske, and G. Masters, A new global crustal model at 5x5 degrees: CRUST-5.0, *EOS, Trans. Am. Geophys. Soc.*, 76, 421, 1995.

Nelder, J. A. and R. Mead, 1965. A simplex method for function minimization, *Computer Journal*, 7, 308–313, 1965.

Su, W.-J. and A. M. Dziewonski, Joint 3-D inversion for P- and S-velocity in the mantle (abstract), *EOS, Trans. Am. Geophys. Un.*, 74, 556, 1993.

Su, W.-J., R. L. Woodward and A. M. Dziewonski, Degree-12 Model of Shear Velocity Heterogeneity in the Mantle, *J. Geophys. Res.*, 99, 6945–6980, 1993.

## Appendix

Measurements and Global Models of  
Surface Wave Propagation  
(preprint)

to appear in  
Journal of Geophysical Research

To appear in the *Journal of Geophysical Research*, 1997.

## Measurements and global models of surface wave propagation

Göran Ekström, Jeroen Tromp, and Erik W. F. Larson

Department of Earth and Planetary Sciences, Harvard University, Cambridge, Massachusetts

### Abstract

A new technique for making single-station phase velocity measurements is developed and applied to a large number of globally recorded Rayleigh and Love waves in the period range 35–150 s. The method is based on phase-matched filter theory and iteratively suppresses the effect of interfering overtones by minimizing residual dispersion. The model surface wave signal is described by its amplitude and apparent phase velocity, both of which are parameterized in terms of smooth B-spline functions of frequency. A misfit function is constructed which represents the difference between the model and observed waveforms, and the optimal spline coefficients are estimated in an iterative misfit minimization algorithm. In order to eliminate cycle skips in the measurements of phase at short periods, the waveforms are first matched at long periods, and the frequency range is gradually extended to include higher frequencies. The application of the algorithm to records from the Global Seismographic Network, using earthquakes in the Harvard centroid-moment tensor catalog, results in the determination of more than 50,000 high-quality dispersion curves. The observed variations in measured dispersion for pairwise similar paths are used to estimate realistic uncertainties in the data. Phase delays at discrete periods are inverted for global maps of variations in phase velocity expanded in spherical harmonics up to degree 40. A realistic resolution test indicates that structures are well recovered up to at least degree 20. The new phase velocity maps explain 70–96% of the observed variance in phase residuals, reflecting the high internal consistency of the dispersion measurements.

## Introduction

Regional variations in the propagation speeds of teleseismic surface waves have been noted since the early part of the century [Tams, 1921a, b]. In the 1960s, the magnitudes of these global variations for waves in the period range 10–150 s could be summarized and discussed in terms of gross lateral differences in the layering and structure of the crust and upper mantle [e.g., Oliver, 1962; Deeman, 1969]. Variations at longer periods were also observed and interpreted in terms of lateral variations of upper mantle elastic and anelastic structure [e.g., Toksöz and Anderson, 1966; Kanamori, 1970; Dziewonski, 1971; Wu, 1972]. With the start of digital data collection from new global seismograph networks [Agnew et al., 1976; Peterson et al., 1976] and the development of new techniques for analyzing surface wave dispersion through waveform inversion [e.g., Dziewonski and Stein, 1982], efforts began to map the global variations in long-period phase velocities and the corresponding three-dimensional (3-D) structure of the Earth using tomographic techniques [Masters et al., 1982; Nakanishi and Anderson, 1982, 1983, 1984; Woodhouse and Dziewonski, 1984; Tanimoto and Anderson, 1985; Nataf et al., 1986; Tanimoto, 1986; Wong, 1989; Montagner and Tanimoto, 1990, 1991]. These studies have made use of a variety of seismic data to image the Earth's interior; surface waves have, however, provided the most valuable constraints on upper mantle structure.

Although good recordings of intermediate-period surface waves are much more common than good very long-period recordings, the shortest-period surface waves included in the global tomographic studies referenced above is 75 s, and most of the studies only considered surface waves with periods greater than 150 s. Two explanations for this situation can be found. First, while shorter-period surface waves are sensitive to velocity variations in the shallow mantle, they also depend critically on the structure and thickness of the crust, which are not very well known on the global scale. By limiting surface wave observations to periods which have less sensitivity to the crust and by applying simple a priori crustal corrections to the data, these studies have sought to eliminate crustal effects. Second, it is more difficult to measure the dispersion of surface waves at intermediate periods than at long periods. In particular, establishment of the total propagation phase of a teleseismic surface wave at a particular period, such that there is no remaining ambiguity in the integral number of cycles,

is a nontrivial task.

There are, in addition, several complicating aspects of surface wave propagation in a laterally heterogeneous Earth which are more significant for shorter-period waves, but which are not very well understood or predicted, such as focusing, refraction of the apparent ray path, and scattering [e.g., Evernden, 1954; Capon, 1970; Sobel and von Seggern, 1978; Lay and Kanamori, 1985; Woodhouse and Wong, 1986; Laske, 1995]. These complications usually do not prevent us from making measurements of dispersion but do suggest that the interpretation of these measurements in terms of Earth structure will depend on whether the chosen theoretical model for surface wave propagation in a heterogeneous Earth is adequate.

Recently, interest in incorporating shorter-period surface waves in global studies has grown [Trampert and Woodhouse, 1995, 1996; Zhang and Lay, 1996; Laske and Masters, 1996; Ekström and Dziewonski, 1995]. This is primarily due to the high resolving power, both radially and laterally, that these waves can afford in the shallowest mantle. Careful investigation of these waves can help resolve some difficult geodynamical questions, such as the issue of “passive” (shallow) versus “active” (deep) mechanisms for spreading at mid-ocean ridges [Zhang and Tanimoto, 1992; Su et al., 1992] and the depth extent and chemical versus thermal nature of lithospheric roots under parts of the continents [Jordan, 1975].

In addition to providing information about the elastic and anelastic structure of the crust and shallow mantle, intermediate-period surface waves are important for earthquake source studies. For shallow earthquakes, surface waves are commonly the largest teleseismic phases recorded on long-period seismograms. For recordings with a low signal-to-noise ratio, they may be the only part of the seismogram that can be used for a source mechanism determination. Improvements in our ability to model global surface wave propagation at shorter periods will make it possible to routinely derive source geometries and moments for earthquakes in the magnitude range  $4.5 \leq M \leq 5.0$ , something which is now feasible only in areas where there is access to regional or local data. It is worth noting that for this application, the interpretation of the dispersion in terms of a 3-D Earth model is of less importance.

In this paper, our first objective is to present a new analysis algorithm which overcomes the difficulty of determining the absolute propagation phase for highly dispersed intermediate-period surface waves.

Our second objective is to present the data set of dispersion measurements and associated realistic uncertainties which has resulted from the systematic application of the new algorithm to a very large volume of global digital data. Our final objective is to derive and present phase velocity maps, which can be used to model global surface wave propagation in the period range 35–150 s, as well as, in future studies, to infer the 3-D structure of the shallow mantle.

## Theory

We describe and interpret the propagation of fundamental Love and Rayleigh waves using ray theory on a sphere [e.g., *Tromp and Dahlen*, 1992, 1993] and write the surface wave seismogram  $u(\omega)$  as

$$u(\omega) = A(\omega) \exp[i\Phi(\omega)], \quad (1)$$

where  $A(\omega)$  and  $\Phi(\omega)$  are the amplitude and phase, respectively, of the wave as functions of the angular frequency  $\omega$ . For a given source-receiver geometry, the phase  $\Phi$  is the sum of four terms,

$$\Phi = \Phi_S + \Phi_R + \Phi_C + \Phi_P, \quad (2)$$

where  $\Phi_S$  is the source phase calculated from the source mechanism and geometrical ray takeoff azimuth,  $\Phi_R$  is the receiver phase,  $\Phi_C$  is the static phase contribution from each ray focus, and  $\Phi_P$  is the propagation phase

$$\Phi_P(\omega) = \int \frac{\omega}{c(\omega)} ds, \quad (3)$$

where  $c$  is the local phase velocity and the integration follows the ray path. The amplitude  $A$  can be expressed as

$$A = A_S A_R A_\Delta A_Q, \quad (4)$$

where  $A_S$  is the excitation at the source,  $A_R$  is the receiver amplitude,  $A_\Delta$  is the geometrical spreading factor, and  $A_Q$  is the decay factor due to attenuation along the ray path. When the location and focal mechanism of the earthquake are known, a theoretical reference seismogram  $u^0(\omega)$  based on a spherical Earth model can be calculated and written as

$$u^0(\omega) = A^0(\omega) \exp[i\Phi^0(\omega)]. \quad (5)$$

The propagation phase for the reference surface wave is

$$\Phi_P^0(\omega) = \frac{\omega R \Delta}{c^0} = \frac{\omega X}{c^0}, \quad (6)$$

where  $c^0$  is the spherical Earth phase velocity,  $\Delta$  is the angular epicentral distance,  $R$  is the radius of the Earth, and  $X$  is the propagation path length measured along the great circle. We express the observed surface wave  $u(\omega)$  as a perturbation with respect to the reference seismogram

$$u(\omega) = [A^0(\omega) + \delta A(\omega)] \exp[i\Phi^0(\omega) + \delta\Phi(\omega)]. \quad (7)$$

Attributing  $\delta\Phi$  to a perturbation of the propagation phase, we have

$$\Phi_P = \Phi_P^0 + \delta\Phi = \frac{\omega X}{c^0 + \bar{\delta}c}, \quad (8)$$

where  $\bar{\delta}c$  is the apparent average phase velocity perturbation, calculated for the distance  $X$  along the great circle.

In order to find an adequate and simple model parameterization for a realistic observed surface wave shape, we assume that the phase and amplitude of Love and Rayleigh waves vary smoothly with frequency and that discontinuities in the phase, which can result, for example, from multipathing, are rare. Evidence for refraction and multipathing at periods shorter than 30 s is not uncommon [e.g., *Lerner-Lam and Park*, 1989; *Levshin et al.*, 1992], but our experience is that a smooth parameterization of phase and amplitude is sufficient to model most of the observations. We therefore express the amplitudes as

$$A(\omega) = b_0 \sum_{i=1}^N b_i f_i(\omega), \quad (9)$$

where  $b_i$  ( $i = 1, 2, \dots, N$ ) are spline coefficients for the cubic B-spline polynomials  $f_i$  (see Figure 1) and  $b_0$  is a constant. Initially, the coefficients  $b_i$  are calculated for a reference Earth model and normalized such that

$$\frac{1}{N} \sum_{i=1}^N |b_i| = 1. \quad (10)$$

The propagation phase  $\Phi_P$  is a rapidly growing function of  $\omega$  and therefore not easily splined. Instead, we spline the apparent average phase velocity perturbation  $\bar{\delta}c$

$$\bar{\delta}c(\omega) = \sum_{i=1}^N d_i f_i(\omega), \quad (11)$$

where  $f_i$  are the same cubic B-spline polynomials as above and  $d_i$  are spline coefficients to be determined for each path.

This parameterization will not be adequate for all observations. For example, for paths along which multipathing or scattering is severe, we will not achieve a good agreement between the observed seismogram and this model of the signal. However, by applying a selection criterion based on fit between the observed and model signal, we can identify and eliminate many of these paths and corresponding unreliable dispersion measurements.

## Measurement Technique

The objective is to separate out the fundamental mode surface wave in the seismogram and to make a measurement of its dispersion. Real data contain noise, as well as interfering seismic phases, so we need a method which suppresses noise and isolates the fundamental mode surface waves from other phases. Since we will require many measurements, we also need a method which can be automated. Many techniques have been presented for making single-station dispersion measurements; the method we develop builds on the ideas of residual dispersion [Dziewonski and Hales, 1972; Dziewonski et al., 1972] and phase-matched filtering [e.g., Herrin and Goforth, 1977]. Our method adds several features to these two basic concepts.

First, we assume that the observed seismogram contains a dispersed surface wave signal  $A^S(\omega) \exp[i\Phi^S(\omega)]$ , where the  $S$  superscript refers to the observed signal. The phase-matched filter which will optimally enhance and compress this signal in the presence of white noise is the signal itself [e.g., Herrin and Goforth, 1977]. That is, by autocorrelating the signal, the dispersion is annihilated and the noise is suppressed: the result is a zero-phase filtered spike with amplitude spectrum  $|A^S(\omega)|^2$ .

Second, we consider how to best isolate the fundamental mode from interfering overtones. This is also achieved by correlation with the phase-annihilating filter  $\exp[i\Phi^S(\omega)]$ . However, only the part of the time domain correlation function close to its maximum corresponds to fundamental mode energy. In order to isolate the fundamental mode energy, the part of the correlation function near the maximum can be windowed in time [e.g., Dziewonski et al., 1972; Herrin and Goforth, 1977; Lerner-Lam and Jordan, 1983; Levshin et al., 1992]. If the phase delay is then reintroduced by multiplying the windowed correlation function by  $\exp[\Phi^S(\omega)]$  in the spectral domain, a filtered version of the input signal is obtained, in which

signals with dispersion different from that of the fundamental mode are suppressed. However, there is no single time window which will be optimal for windowing the correlation function. If a broad range of frequencies is considered and the window is selected to include a cycle or more of the longest periods, then the window used will be too wide for high frequencies (thereby including signals that have different group delays) and vice versa.

On the basis of these considerations, we develop the following algorithm for estimating the dispersion and amplitude of the fundamental mode surface wave in the observed signal. A trial fundamental mode model seismogram  $A^M(\omega) \exp[i\phi^M(\omega)]$  is constructed based on the source and receiver locations, the focal mechanism, and the phase and amplitude effects of propagation in the reference Earth model. We then construct the whitening phase-matched filter  $W$

$$W(\omega) = \frac{1}{A^M(\omega)} \exp[i\Phi^M(\omega)], \quad (12)$$

and cross correlate this function with the observed seismogram. If the observed seismogram contained a signal with identical dispersion and amplitude spectrum to our trial synthetic seismogram and if we were considering all frequencies, the result of the cross correlation would be a delta function in time. If we considered a range of frequencies, the result would be a band-passed delta function. The trial dispersion and amplitude will, in general, not match the observed signal, and there will be a misfit. By adjusting the model seismogram to minimize the misfit, an optimal estimate of the dispersion and amplitude in the observed signal is obtained.

The specific misfit function must be chosen with care, and we have found the following approach to be efficient and useful. Consider the full range of frequencies  $[\Omega_{\min}, \Omega_{\max}]$  for which a dispersion and amplitude estimate is to be obtained. In this study, the full period range is 250–32 s. Divide this range into  $2N - 1$  subranges such that

$$\begin{aligned} \omega_{\min}^i &= \Omega_{\min} + (i - 1)\Delta\omega, \\ \omega_{\max}^i &= \Omega_{\min} + (i + 1)\Delta\omega, \end{aligned} \quad (13)$$

for  $i = 1, 2, \dots, 2N - 1$  and  $\Delta\omega = (\Omega_{\max} - \Omega_{\min})/(2N)$ , and construct  $2N - 1$  narrow band-pass filters  $F_i(\omega)$  using Welch tapers [Press et al., 1986] over these ranges (Figure 2). Filter the cross-correlation function in each of these bands,

$$G_i(\omega) = F_i(\omega)S(\omega)W^*(\omega), \quad (14)$$

and do the same to the whitened autocorrelation of the trial synthetic seismogram,

$$\begin{aligned} H_i(\omega) &= F_i(\omega) A^M(\omega) \exp[i\Phi^M(\omega)] W^*(\omega) \\ &= F_i(\omega), \end{aligned} \quad (15)$$

that is, a band-passed delta function. These functions are Fourier transformed back to the time domain to obtain the band-passed cross correlation  $g_i(t)$  and the model autocorrelation  $h_i(t)$  to form the misfit function

$$\Psi(c_k, d_k) = \sum_{i=1}^{2N-1} w_i \frac{\sum_{j=-J_i}^{J_i} [g_i(t_j) - h_i(t_j)]^2}{\sum_{j=-J_i}^{J_i} [h_i(t_j)]^2}, \quad (16)$$

where  $c_k$  and  $d_k$  are the spline coefficients to be varied,  $w_i$  is a weight given to the misfit in the  $i$ th frequency passband, and  $J_i$  is the width (in terms of time point samples) of the time window over which the cross correlations and autocorrelations are compared. We generally choose  $J_i$  to include three cycles of the center period in the passband, that is,  $J_i = 3T/(2\Delta t)$ , where  $T$  is the center period  $4\pi/(\omega_{\max}^i + \omega_{\min}^i)$  and  $\Delta t$  is the sampling interval.

The main difficulty in obtaining dispersion measurements from teleseismically observed surface waves at periods less than about 100 s is that variations in phase velocity are sufficiently large to cause path variations of several cycles in phase, and isolated residual phase measurements in the range  $[-\pi, \pi]$  at a single period are therefore ambiguous in multiples of  $2\pi$ . For minor arc observations, however, phase measurements at periods longer than 100 s can be associated with a total cycle count without difficulty. If a continuous dispersion curve can be anchored at long periods, the total phase perturbation can then be inferred without ambiguity.

In order to obtain the complete broadband dispersion, we therefore employ a method we call iterative frequency band expansion in the minimization of  $\Psi$ . We initially determine the dispersion parameters in a narrow frequency range centered around 100 s and then, in several iterations, increase the higher frequency end of the total frequency range. In each iteration, the dispersion and amplitude parameters are adjusted to minimize  $\Psi$  using the downhill simplex method of *Nelder and Mead* [1965]. Only the frequency bands which fall within the range of considered frequencies are included in the misfit function sum (equation (16)). A search algorithm such as the downhill simplex method is convenient for solving this problem, since it is easy to incorporate constraints

such as nonnegativity of  $A$  and realistic limits on  $\delta c$ . Once  $\Psi$  is minimized for a given frequency range, the range is expanded to include higher frequencies. Because of the smoothness of  $\delta c$ , a prediction can be made for frequencies slightly higher than the ones included in the previous iteration. This ensures that the phase difference between model seismogram and observed seismogram always remains small, so that gradient methods for minimizing  $\Psi$  continue to work in the subsequent iteration.

An example of the minimization procedure is given in Figure 3. The observed seismogram, filtered between 250 and 32 s, is shown together with a model seismogram calculated for the combination of the mantle heterogeneity model SH8U4L8 [*Dziewonski and Woodward*, 1992] and the preliminary reference Earth model (PREM) [*Dziewonski and Anderson*, 1981]. The two waveforms are quite different, and it is clear that major adjustments are required in both phase and amplitude in order to make them agree. When filtered between 250 and 75 s (Figure 3b) there is better agreement. After adjustment of phase and amplitude in this period range, the two waveforms are very similar (Figure 3c); the frequency window is broadened (Figure 3d); again, the phase and amplitude are adjusted. After five iterations of frequency window expansion, the full waveform is matched (Figure 3e). The resulting dispersion and amplitude perturbations are shown in Figure 4. No damping of the dispersion curve to the starting curve is involved, and the results are largely insensitive to the initial values of  $A$  and  $\delta c$ .

## Application

We have applied the method described in the previous section to digital seismograms from the Global Seismographic Network (GSN) of Incorporated Research Institutions for Seismology (IRIS), the Chinese Digital Seismograph Network (CDSN), the Global Telemetered Seismograph Network (GTSN), and the MEDNET and GEOSCOPE networks, using earthquake sources from the period January 1989 to September 1995. Figure 5 shows the distribution of the earthquakes and stations from which data have been collected.

Analysis was attempted for earthquakes with  $M_W \geq 5.5$ . We used the moment tensors and centroid locations in the Harvard centroid-moment tensor (CMT) catalog [*Dziewonski et al.*, 1981] to calculate the source excitation. Only shallow earthquakes ( $h <$

50 km) were included in order to maximize the excitation of surface waves. In addition, we considered only paths in the distance range  $25^\circ \leq \Delta \leq 150^\circ$  in order to avoid problems inherent in isolating the fundamental mode at short distances and close to the antipode. The variations in  $\delta c$  and  $A$  between 250 s and 32 s were parameterized using six spline basis functions. After several experiments, this number of spline functions was found to be adequate for describing most of the variations seen in the data.

For each seismogram, the instrument response was removed to restore ground displacement. Rayleigh wave dispersion was determined from the vertical component, and Love wave dispersion was determined from transverse records constructed by rotation of the horizontal components using the great circle back azimuth. More than 128,000 station-receiver paths were analyzed, but only a fraction of these yielded useful measurements. For some paths, we obtained good dispersion curves to 45–50 s, but the algorithm was unsuccessful in extending the curve to shorter periods. We therefore accumulated two data sets: a large collection of measurements valid for periods longer than 45 s and a slightly smaller data set extending to the shortest period we considered, 32 s. The quality of each dispersion curve was assessed in various ways, and the value of the misfit function  $\Psi$  was found to provide the best indicator of overall quality. Measurements with  $\Psi > 0.75$  were found to be less reliable and were discarded. This led to a reduction in the number of useful paths to approximately 56,000.

In further analysis of these measurements, the dispersion curves were converted to phase anomalies  $\delta\Phi$  at the discrete periods 150, 100, 75, 60, 50, 45, 40, 37, and 35 s. The maximum and minimum periods correspond roughly to the center frequencies of the first and last misfit bands in equation (16). Owing to the spline parameterization, the phase anomalies at adjacent frequencies are correlated. However, by oversampling the dispersion curve and calculating phase velocity maps at many frequencies, it will in the future be easier to interpolate smooth dispersion curves for arbitrary paths. In the conversion to phase anomaly measurements, an additional quality check was applied by discarding measurements with poor fit in the frequency bands bracketing the desired frequency.

The result of applying these quality constraints is a homogeneous data set of phase anomalies. The number of observations varies depending on the wave type and period and ranges between approximately 15,000 and 38,000 (Table 1). The jump in the number of

observations between the 45 and 50 s measurements is due to the fact that shorter-period observations are derived from the smaller data set of dispersion curves described above. The smaller number of good Love wave observations at 150 s reflects the difficulty of isolating the long-period fundamental mode signal in minor arc measurements at these periods.

In addition to separating “good” measurements from “bad” by imposing strict requirements on the misfit function  $\Psi$  and the fit in individual frequency bands, we attempted to make realistic estimates of the observational uncertainties in our data set. Errors in single-station phase velocity measurements come from several sources. For example, if an earthquake epicenter is poorly known, an error  $\delta X$  in the epicentral distance will lead to a phase error of  $\omega\delta X/c^0$ , which, for a 40 km mislocation and a phase velocity of  $4 \text{ km s}^{-1}$ , leads to a 10 s difference in travel time and to a  $\pi/2$  phase error at 40 s period. Errors in the source phase calculation, due to an incorrect moment tensor or earthquake depth or more subtly as a consequence of the source excitation being calculated in PREM rather than in a local model, can lead to phase errors as large as  $\pi$ . Errors in station timing are also possible, as are methodological errors due to inadequacies of our dispersion measurement algorithm.

Rather than attempting to estimate the probable error distributions for these different effects, we make an empirical estimate of the aggregate uncertainty in our measurements. Owing to the scope of our study, a large number of phase observations correspond to pairwise similar paths. This results primarily from having many earthquakes in one region recorded at an individual station, but there are also some clusters of stations, as in California, which record essentially the same path for a given earthquake.

We first assume that each phase anomaly measurement  $\delta\Phi_i$  for a given path has associated with it an observational error  $\epsilon_i$  which is drawn from a normal distribution with zero mean and standard deviation  $\sigma$ . We next construct a distribution of measurement differences by collecting all pairs of observations which correspond to similar paths and calculate the difference between the two phase measurements. If, in each pair, the two measurements are uncorrelated, the resulting distribution will have a standard deviation of  $2\sigma$ . By calculating the standard deviation of this distribution, we therefore obtain an indirect measure of 2 times the uncertainty in our observations. We note that the uncertainty we estimate in this way is likely to be smaller than the true uncertainty, since it does

not include the effects of systematic errors, for example, in earthquake locations.

For each period that we analyzed, we constructed a distribution of measurement differences, selecting all pairs of paths for which the starting and ending points were within  $3^\circ$  of each other. The standard deviation of this distribution was calculated, and half of this value was assigned as the estimated observational uncertainty in our measurements. Figure 6 shows the distribution of differences for Rayleigh waves at 75 s period. On the basis of our observation that paths with low misfits  $\Psi$  were of a higher quality, we separated the paths into three ranges of  $\Psi$  and thereby obtained three groups of observations with varying quality: The A range ( $0 \leq \Psi \leq 0.25$ ), the B range ( $0.25 < \Psi \leq 0.5$ ), and the C range ( $0.5 < \Psi \leq 0.75$ ), each associated with an empirical uncertainty (Table 2).

## Inversion for Global Phase Velocity Maps

We use the collection of dispersion measurements and the associated uncertainties to derive and compare three models of global surface wave propagation: a simple regionalized model; a low-degree spherical harmonic model obtained by undamped inversion; and a smooth high-degree spherical harmonic model obtained by damped inversion. We make use of the standard approximation that the surface waves have traveled the minor arc along the great circle connecting the source and receiver and do not here explore the possible effects of more complicated propagation paths on a heterogeneous Earth. Earlier studies have concluded that off-great circle propagation effects on the propagation phase usually are small, while effects on takeoff and arrival azimuths and amplitudes can be significant [e.g., *Laske*, 1995].

### A Pure-Path Regionalized Inversion

In order to quantify the quality of fit to our data that can be obtained by a very simple regionalized model of the Earth, we use the dispersion measurements to estimate phase velocities in the six tectonic regions identified by *Jordan* [1981] in the model GTR1. This geographical regionalization provides a gross differentiation between young (A), intermediate age (B), and old oceanic lithosphere (C), as well as between Precambrian shields and platforms (S), Phanerozoic platforms (P), and regions of the continents having been exposed to Phanerozoic deforma-

tion and magmatic activity (Q), where the letters correspond to the labels used by *Jordan* [1981].

We use the pure-path approach to derive regional dispersion curves. The observed phase anomaly is modeled as having accumulated as a result of phase velocity variations in the six tectonic regions,

$$\delta\Phi = -\frac{\omega}{c^0} \sum_{i=1}^6 X^i \frac{\delta c^i}{c^0}, \quad (17)$$

where  $X^i$  is the path length and  $\delta c^i$  is the phase velocity variation in the  $i$ th tectonic region. We have made use of the standard approximation  $1/(1 + \delta c/c^0) \approx 1 - \delta c/c^0$ , which is adequate as long as the velocity variations are small. In order to find the phase velocity variations  $\delta c^i$  which optimally fit the observations, we form the  $\chi^2$  misfit function

$$\chi^2 = \sum_{j=1}^N \frac{1}{\sigma_j^2} \left( \delta\Phi_j - \frac{\omega}{c^0} \sum_{i=1}^6 X_j^i \frac{\delta c^i}{c^0} \right)^2, \quad (18)$$

where  $j$  is the index of the observation,  $N$  is the total number of observations, and  $\sigma_j$  is the associated observational uncertainty.

The misfit function  $\chi^2$  is minimized by straightforward least squares inversion for the six velocity perturbations  $\delta c^i$  with respect to PREM. Figure 7 shows the dispersion curves for Love and Rayleigh waves. The results are similar to those derived in earlier studies, and here we focus on how well the derived regionalized model explains our observations. Figure 8 shows the variance reduction at different periods. The dispersion curves derived for GTR1 explain more than 80% of the Love wave signal at the shortest periods and approximately 70% of the Rayleigh wave signal. This is primarily a consequence of the strong signal generated by the difference between continents and oceans. At longer periods, the variance reduction diminishes, and at 150 s period, less than half of the data variance for both Love and Rayleigh waves is explained by GTR1. This suggests that even though a strong correlation exists, for example, between shields and old oceanic lithosphere and fast phase velocities, this correlation is not sufficient to explain the patterns of anomalies. Figure 9 shows the quantity  $\chi^2/N$ , which provides a measure of how well the model fits the observations, given the estimated uncertainties  $\sigma_i$  (Table 2). For a good model,  $\chi^2/N$  should approach unity. While GTR1 explains a significant fraction of the observed variance in phase velocity, the GTR1 residuals are on average  $\sqrt{5}$  times

greater (for Rayleigh waves) and  $\sqrt{8}$  times greater (for Love waves) than the a priori observational uncertainties.

### Models Expressed in Spherical Harmonics

We now consider a smooth, global parameterization in terms of spherical harmonics. The predicted propagation phase anomaly between a source at  $(\theta_S, \phi_S)$  and a receiver at  $(\theta_R, \phi_R)$  is written

$$\delta\Phi = -\frac{\omega}{c^0} \int_{(\theta_S, \phi_S)}^{(\theta_R, \phi_R)} \frac{\delta c(\theta, \phi)}{c^0} ds, \quad (19)$$

and the phase velocity perturbation is expressed in complex spherical harmonics

$$\frac{\delta c(\theta, \phi)}{c^0} = \sum_{l=0}^L \sum_{m=-l}^{m=l} C_{lm} Y_{lm}(\theta, \phi), \quad (20)$$

where the  $Y_{lm}$  are the fully normalized surface spherical harmonics [Edmonds, 1960] and  $L$  is the maximum degree of the expansion. The misfit function is formulated analogously to equation (18), and we invert for the coefficients  $C_{lm}$ .

The resolution afforded by our large set of observations allows us to invert for models truncated at angular degree  $L = 16$  without applying additional smoothing or regularizations to the solution. We use the results of this undamped, truncated inversion in two ways. First, the resulting models are used to calculate global rms velocity perturbation values at each period,  $\delta c_{\text{rms}}/c^0$ , which we then use to quantify smoothness in our inversion for higher degree structure. We write

$$\frac{\delta c_{\text{rms}}}{c^0} = \left[ \frac{1}{4\pi} \int_S \left( \frac{\delta c}{c^0} \right)^2 d\Omega \right]^{1/2}, \quad (21)$$

which, with  $A_{lm} = \Re(C_{lm})$  and  $B_{lm} = \Im(C_{lm})$ , becomes

$$\frac{\delta c_{\text{rms}}}{c^0} = \left[ \frac{1}{4\pi} \sum_{l=1}^L \left( A_{l0}^2 + \sum_{m=1}^{m=l} 2A_{lm}^2 + 2B_{lm}^2 \right) \right]^{1/2}. \quad (22)$$

Second, we use the  $L = 16$  model to identify outliers, that is, observations which are so poorly predicted by the  $L = 16$  model that we believe that they are erroneous. Fewer than 2% of the data were identified as outliers; these data were not used in the higher-degree inversions. However, for consistency, we continue to include these data in the calculations of misfit and variance reduction.

Not surprisingly, the  $L = 16$  inversions provide a much higher variance reduction and a better fit to the data than does GTR1 (Figure 8). Especially for longer periods, the improvement in variance reduction is very clear, reflecting the lower correlation of mantle velocity anomalies with surface geology. The improvement in fit to the data, expressed as the reduction in size of the average residual, is approximately  $\sqrt{3}$  (Figure 9). Figure 10 shows the resulting global rms velocity variations for the range of periods considered. The effect of the crust is seen in the rapid increase of Love wave rms velocity variations at shorter periods. At 75 s, Love and Rayleigh waves exhibit approximately equal lateral variability.

Regularization of the inversion is required when we determine phase velocity maps expanded to higher angular degrees. Several choices are available for stabilizing the inversion, and we have chosen to minimize a measure of the model roughness, defined as the squared rms gradient of the model. The scaled rms gradient is

$$\mathcal{R} \propto \left[ \int_S \left( \nabla \frac{\delta c}{c^0} \right) \cdot \left( \nabla \frac{\delta c}{c^0} \right) d\Omega \right]^{1/2}, \quad (23)$$

and for our models expanded in spherical harmonics, we calculate  $\mathcal{R}$  as

$$\mathcal{R} = \frac{1}{(\delta c_{\text{rms}}/c^0)} \left[ \frac{1}{4\pi} \sum_{l=1}^L l(l+1) \left( A_{l0}^2 + \sum_{m=1}^{m=l} 2A_{lm}^2 + 2B_{lm}^2 \right) \right]^{1/2}. \quad (24)$$

The effect of smoothing is similar to applying a low-pass filter to the model, and an alternative definition of roughness, such as the squared Laplacian [e.g., Laske and Masters, 1996], corresponds to choosing a different spectral falloff.

We determine the model coefficients which solve the minimization problem

$$\min \left( \frac{\chi^2}{N} + \gamma \mathcal{R}^2 \right), \quad (25)$$

where  $\gamma$  is a damping parameter which needs to be chosen. Through scaling of the gradient by  $(\delta c_{\text{rms}}/c^0)^{-1}$ , we compensate for the fact that shorter-period maps, because of their greater amplitude variations, also have larger gradients. This scaling allows us to use the same damping parameter  $\gamma$  at all periods. The choice of  $\gamma$  is usually based on an examination of the

trade-off curve between misfit and either the size or the roughness of the resulting model. Our choice is based on these considerations, aided by our subjective judgment of what constitutes a reasonable level of roughness. Figure 11 shows a representative trade-off curve and indicates the solution which corresponds to our final choice for  $\gamma$ .

Plates 1a and 1b show the resulting Love and Rayleigh wave phase velocity perturbation maps at 35, 50, 75, and 150 s period. Many of the features apparent in these maps have been seen in earlier studies as well and have been related to global tectonic features. For example, there are strong signals associated with, at shorter periods, the contrast between continents and oceans and, at all periods, slow velocities near Iceland and the Red Sea rift zone. The expected pattern of increasing velocities in the ocean basins, related to the cooling of the oceanic lithosphere, is also clearly apparent. Our maps offer a sharper definition of many features, allowing for a firmer association between observed anomalies and specific tectonic elements. For example, for Love waves at 150 s and Rayleigh waves at 75 s, we see a strong correlation between fast velocities and the oldest cratons and the distinct separation of these anomalies along Proterozoic orogens; note the separation of the West Africa, Congo, and Kalahari cratons. Another interesting feature of the maps is the slow anomalies in the Pacific Ocean, away from the ridges, seen most prominently at the longest periods. A detailed interpretation of the many intriguing features identifiable in these maps of phase velocity, particularly in terms of a 3-D velocity model for the upper mantle, will be presented in a separate paper.

Table 3 gives the integral measures of rms level of the models and the model gradients for the  $L = 40$ , the  $L = 16$ , and other models, allowing for a comparison of their amplitude and roughness. The correlations between the  $L = 40$  and  $L = 16$  maps are very high and vary from 0.95 to 0.99 depending on the period and wave type (Table 4). These high values are, to a large extent, due to the fact that the heterogeneity in the maps is dominated by low-degree structures. However, correlations for individual degrees are also high, ranging from 0.67–1.00. For  $0 \leq l \leq 8$ , the correlations are all greater than 0.95.

The model coefficients are not tabulated here, but they can be obtained directly from the authors or in electronic form via anonymous ftp at [saf.harvard.edu](http://saf.harvard.edu), by retrieving the files in pub/ETL-JGR-96. The tabulated values are  $A_{lm}$  and  $B_{lm}$  for  $m \geq 0$ .

## A Resolution Test

It is evident from Figures 8 and 9 that the improvement in variance reduction and data fit that correspond to going from the  $L = 16$  (289 parameters) models to the  $L = 40$  (1681 parameters) models is modest, and it is therefore necessary to justify the added model complexity. We performed several standard resolution experiments, which showed that the geometry and amplitude of low-degree ( $l \leq 12$ ) structure is essentially completely recovered in the inversions. Higher-degree structure is recovered better in the northern than in the southern hemisphere, reflecting the ray coverage. The geometry of higher-degree structure is generally preserved, but the damping used in the inversion, as well as the intrinsic path-averaging effect of surface wave dispersion observations, lead to a smearing and reduction in amplitude of shorter-wavelength features. These general conclusions are well illustrated by the following test in which we attempted to resolve a realistic phase velocity map based on an a priori model of the crust.

The thickness and velocity structure of the crust contribute significantly to the dispersion of surface waves, in particular, at shorter periods. Recently, *Mooney et al.* [1995] compiled a detailed preliminary global crustal structure model, CRUST-5.0, with  $5^\circ$  by  $5^\circ$  resolution. We calculated the dispersion predicted by this model by substituting the CRUST-5.0 values ( $v_P$ ,  $v_S$ , and  $\rho$ ) into PREM, adjusting also the depth of the Moho and accounting for topography and bathymetry. We then evaluated the surface wave dispersion in each modified local Earth structure. The  $5^\circ$  by  $5^\circ$  global dispersion map that resulted was then expanded in spherical harmonics up to degree  $l = 40$ . Figure 12 shows the phase velocity map thus calculated for Love waves at 35 s period.

For the collection of paths that were used in our inversions, we next calculated the corresponding phase anomalies for propagation in the synthetic model. To each observation, we added Gaussian noise, corresponding to the uncertainty  $\sigma_i$  associated with each path, multiplied by a factor of 2 in order to mimic the quality of fit obtained using the real data. We then inverted the simulated data using the same damping  $\gamma$  as was used in the inversion of the real observations. We achieved a 96% variance reduction and  $\chi^2/N=1.84$ , similar to what we obtained for the real data (Figures 8 and 9).

Figure 12 shows the inversion results for Love waves at 35 s period. There is very good agreement

between the input and retrieved maps, in particular, in the northern hemisphere. An area which shows clear indications of smearing is the Andes mountains, where the narrow band of north-south trending slow velocities is poorly recovered. In contrast, slow velocities corresponding to areas of thick crust and deep basins in Eurasia are very well recovered. The essentially uniform velocity of the ocean basins is reasonably well recovered, with spurious variations not exceeding  $\pm 1.5\%$  (corresponding to approximately 10% of the full range of variations seen in the map). Figure 13 shows a comparison of the spectral powers of the input and retrieved models, as well as the correlation coefficient for each spherical harmonic degree. The power in the input model is well recovered up to  $l = 12$ , and for higher angular degrees, the retrieved model underestimates the power by a factor as high as 3. The correlation between input and retrieved models is greater than 0.5 for  $l \leq 36$ . Since we have fewer observations for Love waves at 35 s than for any other inversion, we believe that this test provides a good indication of how well we recover the true phase velocity variations in the Earth.

## Discussion

Plate 1 and the corresponding spherical harmonic coefficients represent the primary results of our study. Interpretation of these results in terms of 3-D Earth structure will be presented elsewhere. Here we limit our discussion to (1) the discrepancy between our global, average phase velocities and those of PREM, (2) a comparison of our maps with the effects of crustal structure, and (3) comparisons with other recent studies of intermediate-period global phase velocity variations.

### Spherically Symmetric Term

The results of our study indicate that the spherical average phase velocities predicted by PREM require large corrections. Figure 14 shows the spherical average perturbation for Love and Rayleigh waves at different periods, calculated from the  $A_{00}$  term in the spherical harmonic expansions. For Rayleigh waves around 50 s, the correction required is about 0.8% which is nearly half of the observed rms variation (Figure 14). We note that the sign of the correction is the same as that observed between data used to derive PREM and PREM predictions [Dziewonski and Anderson, 1981]. However, using these new data, the magnitude of the difference is greater. While there

are many possible explanations for the observed discrepancy, we suggest that since the Love wave data are fit quite well by PREM and the Rayleigh waves are significantly faster than predicted, the transverse anisotropy at the top of the mantle may not be as strong as in PREM, where it reaches 5% just below the Moho. Other explanations related, for example, to the global average crustal structure, are of course also plausible. In this article, we have not included the spherically symmetric term in the calculations of rms values, variance reductions, or correlations between models.

### Effect of the Crust

In tomographic studies of the Earth's mantle, surface wave dispersion measurements and phase velocity maps are commonly used to constrain upper mantle velocity variations. For this use, it is necessary to account for crustal effects on the observations before inferring from them the nature of the deeper structure. This is commonly done by subtracting out the predicted effects of an a priori crustal structure, often one which corresponds to the average oceanic or continental crust. The crustal signal is strong for shorter-period waves and decreases at longer periods. Since the rms variations in observed phase velocities also decrease with increasing period, it is not clear, however, that the relative size of the crustal signal decreases with increasing period. We use the model predictions based on Mooney *et al.*'s [1995] crustal model, described above, to investigate this relationship.

The correlation between observed phase velocities and those due to the crust (Figure 15a) follows the expected trend of a greater effect at short periods and for Love waves. The 0.83 correlation for Love waves at 35 s shows that while Love waves, even at this period, have some sensitivity to mantle structure, the observed variations are dominated by the crust. The good agreement in the patterns of the "observed" and "predicted" maps is also seen in the amplitudes of their rms variations; the rms variation (Figure 15b) in the map predicted from CRUST-5.0 is 4.48% and from the inverted phase velocity maps is 3.91%. In addition, the rms gradient of our model  $R = 78.5$  is similar to the  $R = 91.0$  we find for the crustal model.

The correlation with the crustal model decreases with increasing period, and for periods longer than 50 s for Rayleigh waves and 100 s for Love waves, the correlation is negative (Figure 15a). When we calculate the correlation for continental regions only, it is seen to deteriorate faster with increasing period,

so that for Rayleigh waves, the correlation becomes negative at around 45 s, presumably reflecting a lack of correlation between the thickness of the continental crust and the seismic velocities of the underlying mantle.

Figures 15b and 15c compare the rms levels of our phase velocity maps with those of the crustal model riding on a spherically symmetric mantle. Also shown is the rms variation of the residual model which is obtained if the crustal phase velocity maps (as derived from Mooney *et al.*'s [1995] model) are subtracted from our observed maps. The level of heterogeneity seen for Love waves is similar to that which we would expect from the crust alone. Of course, because of the lack of correlation at longer periods, there is a mantle signal in the observed maps, but it is not dominant. For Rayleigh waves, the observed phase velocity variations are greater than those due only to the crust, but it is interesting to note that the level of variations is most similar at the limits of our period interval. This suggests that the details of the crustal correction that are applied in tomographic inversions for 3-D structure are important not only at short periods but also at 100 s and greater periods.

### Comparison With Other Studies

Several groups are pursuing research similar to that presented here, and it is useful to compare our results with other published studies. At periods longer than 80 s, there exists a long history of global phase velocity models, but since many of the earlier studies have been superseded by new and more complete studies, we limit the comparisons to four recent studies: *Trampert and Woodhouse* [1995, 1996], *Zhang and Lay* [1996], and *Laske and Masters* [1996]. In particular, the two studies by Trampert and Woodhouse are similar in scope to the work presented here. *Trampert and Woodhouse* [1995] applied an automatic algorithm to analyze the dispersion of a large number of surface waves and derived global phase velocity maps expanded up to spherical harmonic degree  $l = 40$ . A difference in the data used between our studies is that *Trampert and Woodhouse* [1995, 1996] used both minor and major arc arrivals, while we use only the minor arc. We derive results to 35 s period, while *Trampert and Woodhouse's* [1995, 1996] shortest period is 40 s. In the inversion for phase velocity maps, Trampert and Woodhouse regularized the solution by minimizing the squared Laplacian, in contrast to our choice of minimizing the squared gradient. In their two papers, in 1995 and 1996, results are presented

for 40, 60, 80, 100, and 150 s periods for Love and Rayleigh waves. The primary differences between the two Trampert and Woodhouse studies are the quality and quantity of data included in the inversions and the level of damping. The 1996 results are less damped and consequently rougher. Since our results are in better agreement with the earlier results, we make comparisons with both studies. *Zhang and Lay* [1996] derived phase velocity maps between 85 and 250 s using both minor and major arc data. We compare our results with theirs at 100 s and 150 s. *Laske and Masters* [1996] similarly derived maps between ~75 and 250 s. We compare our maps with theirs at 75, 100, and 150 s.

Table 3 gives the rms and rms gradient values for the various maps, and Table 4 summarizes their correlations with our preferred  $L = 40$  maps. For Love waves at 100 and 150 s, the three maps by *Zhang and Lay* [1996], *Laske and Masters* [1996], and *Trampert and Woodhouse* [1995] correlate equally well with our maps. No two maps from these three studies correlate better than they do individually with our map. For Rayleigh waves, our results have the best correlation with Laske and Masters's results. As can be seen, we have consistently better agreement with Trampert and Woodhouse's 1995 study than with the 1996 study.

The correlation of *Trampert and Woodhouse's* [1996] Love wave map at 40 s period with ours is 0.80, suggesting a relatively good agreement between the two models. However, it is worth noting that we obtained an almost equally good correlation (0.79) between our map and that predicted from the a priori crustal model (see Figure 15). Thus the correlation between the two results is primarily due to the large-scale spatial pattern of oceanic and continental crust, and there exist significant disagreements between the two maps concerning smaller structures. Figure 16 shows the correlation between the two models for different angular degrees in the spherical harmonic expansion. The correlations between the two models start to diverge for degrees as low as  $l = 7$ , and while they remain positive for most angular degrees, they approach zero for the highest degrees.

We believe that, at shorter periods, our results offer an improvement over the models of *Trampert and Woodhouse* [1995, 1996], based on two observations. First, the reductions in variance reported by Trampert and Woodhouse are low in comparison with what we obtain in our study. For example, we obtain a variance reduction of 96% of our Love wave observations

at 40 s period, while Trampert and Woodhouse in their 1995 and 1996 studies report 86% and 77%, respectively. In fact, the fits that their models provide to our data are better (90% and 87%, respectively) than their reported values. This, to us, provides a strong suggestion that their raw measurements are significantly noisier than ours and internally less consistent, perhaps suggesting a problem with the measurement technique.

The second observation we make is that while in many regions there is a striking similarity between our two models, there are some areas where there is strong disagreement, and we believe our result is more realistic. Figure 17 shows a comparison between two Love wave maps at 40 s for India and central Asia, a region which contains the largest elevated plateau and the thickest crust on Earth. These geological features are reflected in our map by the extremely slow phase velocity across Tibet and the continuous band of slow velocities along the Alpine-Himalayan belt of thickened and tectonically active crust. In *Trampert and Woodhouse's* [1996] map and similarly in their 1995 study, the Tibetan plateau is not as prominent a feature, and it is cut and truncated by a fast anomaly at approximately 85°E. On the basis of what is known about the crust and tectonics for this region (see Figure 12), as well as the results from tomographic studies [e.g., *Bourjot and Romanowicz*, 1992], it appears highly unlikely that Trampert and Woodhouse's fast anomaly is a real feature of the Earth. The fact that southern Eurasia is quite well sampled by crossing wave paths in both studies also suggests that the differences are not due to limited resolution but are instead due to errors in the measurements.

## Conclusions

We have developed a new algorithm for making automated phase measurements of dispersed surface waves. By insisting that the surface wave signal should have a smoothly varying phase and amplitude and by anchoring the dispersion curve at a period where there is no ambiguity in the total phase, the new method yields robust measurements of phase for Love and Rayleigh waves with periods as short as 35 s. It is noteworthy that some of these phases exhibit phase delays or advances of as many as 10 cycles ( $\pm 350$  s). The potential exists for applying this algorithm to higher frequencies as well, which might be of particular use for analysis of recordings at regional distances.

The systematic application of our algorithm to teleseismic data from the Global Seismographic Network has yielded a very large database of dispersion and amplitude measurements. By comparing results corresponding to similar paths, we have been able to estimate the uncertainties in our observations. These uncertainties are useful, since without them it is easy to erroneously conclude that a given model provides a good fit to the data based on a high variance reduction. For example, one might be led to believe that the simple regionalization GTR1 provides a good fit to shorter-period surface waves since it reduces the variance by 65–85% (Figure 7). In fact, while GTR1 explains a large fraction of the signal in the data at short periods, primarily due to the large contrast between continental and oceanic structures, the fit it provides to the observations is mediocre at all periods. Knowledge of the approximate true uncertainties in our data also allowed us to assess the resolution and recovery of true Earth structures through a realistic synthetic test (Figures 12 and 13). Our conclusions differ substantially from those of *Ricard et al.* [1996], who performed a similar test using the a priori model 3SMAC [*Nataf and Ricard*, 1996] and a different path coverage. *Ricard et al.* [1996] obtained a very low recovery of power in degrees greater than 10 and only a 53% recovery of the signal for degree 3. They concluded, in agreement with some previous studies [*Mochizuki*, 1993; *Snieder*, 1993; *Nolet et al.*, 1994], that the spectrum of lateral heterogeneity cannot be deduced for degrees higher than 10 using global surface wave tomography. In contrast, we obtain good recovery of structures (Figure 13) to at least degree 20 and essentially complete recovery of the structure up to degree 12. While we do underestimate the power of higher order structures, this is not as severe a problem as implied by the above authors. We agree, however, that the best way to achieve better recovery of shorter-wavelength structures is to include observations corresponding to shorter paths, provided the difficulties of making these measurements are overcome. In addition, data which are more sensitive to gradients in the models, such as polarization angles and amplitudes, could help improve the resolution of smaller-scale structures [*Laske and Masters*, 1996].

A central contribution of this paper is the phase velocity maps. These were derived using several simplifying assumptions. First, we assumed that the phase measurements could be interpreted using the unperturbed great circle path. Clearly, this assumption is easily challenged, given the level of heterogeneity re-

trieved, for example, for 40 s Love waves in Tibet (Figure 17). On the basis of ray-tracing experiments, we do not believe that taking more accurate account of the refraction caused by such heterogeneity will affect the larger-scale features in our models. It is clear, however, that for certain paths, such as those crossing Tibet or grazing continent-ocean margins, the systematic bending of rays into slow areas may affect the mapping of boundaries and smaller-scale features. Further research is needed to investigate the potential bias introduced by this simplifying assumption in specific areas.

A second important assumption is that the observed dispersion can be explained by isotropic variations in phase velocity. Several previous studies have concluded that azimuthal anisotropy contributes significantly to the observed variability in surface wave dispersion, in particular, for Rayleigh waves traversing oceanic lithosphere [e.g., *Forsyth*, 1975; *Tanimoto and Anderson*, 1985; *Nishimura and Forsyth*, 1988; *Montagner and Tanimoto*, 1990]. With the database collected in this study, we are currently investigating the effect of azimuthal anisotropy. Like previous investigators, we find that the main difficulty lies in distinguishing between isotropic and anisotropic heterogeneity in areas with poor path coverage. Results from this investigation will be presented elsewhere. Here it suffices to say that the good fit to the data that can be achieved without accounting for anisotropy suggests that anisotropy, while probably important in certain regions, remains a second-order effect when considering a global data set.

Notwithstanding the need to investigate further the limitations of the simplifying assumptions employed in our inversions, the phase velocity maps derived here provide very good fits to the global data set we have collected. The maps can therefore also be used to predict the phase of teleseismic surface waves, something which will be useful for earthquake studies. The most important use for these maps and the dispersion data is, however, in the determination of the 3-D structure of the upper mantle. Preliminary analysis of our data set in the development of a model expanded up to degree 20 in the upper mantle [*Eckström and Dziewonski*, 1995, 1996] indicates that our measurements of Love and Rayleigh wave dispersion are consistent with previous data sets but that they require higher amplitudes of lateral heterogeneity in the shallowest mantle than seen in previous Harvard mantle models [e.g., *Su et al.*, 1994].

The experiments described above have shown that

the crustal signal in the phase velocity maps is significant and that it must be adequately removed before inferring the structure of the uppermost mantle. While *Mooney et al.*'s [1995] model clearly gives a better picture of the global crust than any we have had previously, the differences between Figures 12 and 17 appear to be difficult to explain without adjustments to the crustal structure. A future inversion of our data which simultaneously adjusts both crustal and mantle 3-D structure therefore seems most desirable.

**Acknowledgments.** We thank A. M. Dziewonski for many helpful discussions, B. Romanowicz, J.-P. Montagner, and H.-C. Nataf for helpful comments on an earlier version of the manuscript, and M. Nettles, S. Sianissian, and M. P. Salganik for help with building and maintaining the seismogram and earthquake databases at Harvard. We are grateful to G. Laske, W. D. Mooney, Y.-S. Zhang, and J. Trampert for making their respective models available to us. The research described here was performed using data from the IRIS, GEOSCOPE, MEDNET, CDSN, and GTSN seismograph networks and was principally supported by AFOSR contract F49620-92-J-0392 and NSF grant EAR-92-19361. Additional support was provided by NSF grant EAR-92-19239, the David and Lucile Packard Foundation, and an NSF Graduate Fellowship.

## References

Agnew, D., J. Berger, R. Buland, W. Farrell, and F. Gilbert, International deployment of accelerometers: A network for very long period seismology, *Eos Trans. AGU*, 57(4), 180–188, 1976.

Bourjot, L., and B. Romanowicz, Crust and upper mantle tomography in Tibet using surface waves, *Geophys. Res. Lett.*, 19, 881–884, 1992.

Capon, J., Analysis of Rayleigh wave multipath propagation at LASA, *Bull. Seismol. Soc. Am.*, 60, 1701–1731, 1970.

Dorman, J., Seismic surface-wave data on the upper mantle, in *The Earth's Crust and Upper Mantle*, *Geophys. Monogr. Ser.*, vol. 13, edited by P. J. Hart, pp. 230–242, AGU, Washington, D. C., 1969.

Dziewonski, A. M., Upper mantle models from “pure path” dispersion data, *J. Geophys. Res.*, 76, 2587–2601, 1971.

Dziewonski, A. M., and D. L. Anderson, Preliminary Reference Earth Model (PREM), *Phys. Earth Planet. Inter.*, 25, 289–325, 1981.

Dziewonski, A. M., and A. L. Hales, Numerical analysis of dispersed seismic waves, in *Methods in Computational Physics*, vol. 11, pp. 39–85, Academic, New York, 1972.

Dziewonski, A. M., and J. M. Stein, Dispersion and attenuation of mantle waves through waveform inversion, *Geophys. J. R. Astron. Soc.*, 70, 503–527, 1982.

Dziewonski, A. M., and R. L. Woodward, Acoustic imaging at the planetary scale, in *Acoustical Imaging*, edited by H. Emert and H.-P. Harjes, vol. 19, pp. 785–797, Plenum, New York, 1992.

Dziewonski, A. M., J. Mills, and S. Bloch, Residual dispersion measurements – A new method of surface wave analysis, *Bull. Seismol. Soc. Am.*, 62, 129–139, 1972.

Dziewonski, A. M., T.-A. Chou, and J. H. Woodhouse, Determination of earthquake source parameters from waveform data for studies of global and regional seismicity, *J. Geophys. Res.*, 86, 2825–2852, 1981.

Edmonds, A. R., *Angular Momentum in Quantum Mechanics*, Princeton Univ. Press, Princeton, N. J., 1960.

Ekström, G., and A. M. Dziewonski, Improved models of upper mantle *S* velocity structure (abstract), *Eos Trans. AGU*, 76(46), Fall Meet. Suppl., F421, 1995.

Ekström, G., and A. M. Dziewonski, Imaging upper mantle *S* velocity structure: Compatibility of different data sets (abstract), *Eos Trans. AGU*, 77(46), Fall Meet. Suppl., F483, 1996.

Everden, J., Direction of approach of Rayleigh waves and related phenomena. II, *Bull. Seismol. Soc. Am.*, 44, 159–184, 1954.

Forsyth, D. W., The early structural evolution and anisotropy of the oceanic upper mantle, *Geophys. J. R. Astron. Soc.*, 43, 103–162, 1975.

Herrin, E., and T. Goforth, Phase matched filters: application to the study of Rayleigh waves, *Bull. Seismol. Soc. Am.*, 67, 1259–1275, 1977.

Jordan, T. H., The continental tectosphere, *Rev. Geophys.*, 13, 1–12, 1975.

Jordan, T. H., Global tectonic regionalization for seismological data analysis, *Bull. Seismol. Soc. Am.*, 71, 1131–1141, 1981.

Kanamori, H., Velocity and *Q* of mantle waves, *Phys. Earth Planet. Inter.*, 2, 259–275, 1970.

Laske, G., Global observations of off-great-circle propagation of long-period surface waves, *Geophys. J. Int.*, 123, 245–259, 1995.

Laske, G., and G. Masters, Constraints on global phase velocity maps from long-period polarization data, *J. Geophys. Res.*, 101, 16,059–16,075, 1996.

Lay, T., and H. Kanamori, Geometric effects of global lateral heterogeneity on long-period surface wave propagation, *J. Geophys. Res.*, 90, 605–621, 1985.

Lerner-Lam, A. L., and T. H. Jordan, Earth structure from fundamental and higher-mode waveform analysis, *Geophys. J. R. Astron. Soc.*, 75, 759–797, 1983.

Lerner-Lam, A. L., and J. J. Park, Frequency-dependent refraction and multipathing of 10–100 second surface waves in the western Pacific, *Geophys. Res. Lett.*, 16, 527–530, 1989.

Levshin, A., L. Ratnikova, and J. Berger, Peculiarities of surface-wave propagation across central Eurasia, *Bull. Seismol. Soc. Am.*, 82, 2464–2493, 1992.

Masters, G., T. H. Jordan, P. G. Silver, and F. Gilbert, Aspherical Earth structure from fundamental spheroidal mode data, *Nature*, 298, 609–613, 1982.

Mochizuki, E., Spherical harmonics analysis in terms of line integrals, *Phys. Earth Planet. Inter.*, 76, 97–101, 1993.

Montagner, J.-P., and T. Tanimoto, Global anisotropy in the upper mantle inferred from the regionalization of phase velocities, *J. Geophys. Res.*, 95, 4794–4819, 1990.

Montagner, J.-P., and T. Tanimoto, Global upper mantle tomography of seismic velocities and anisotropies, *J. Geophys. Res.*, 96, 20,337–20,351, 1991.

Mooney, W. D., G. Laske, and G. Masters, A new global crustal model at 5x5 degrees: CRUST-5.0 (abstract), *Eos Trans. AGU*, 76(46), Fall Meet. Suppl., F421, 1995.

Nakanishi, I., and D. L. Anderson, World-wide distribution of group velocity of mantle Rayleigh waves as determined by spherical harmonic inversion, *Bull. Seismol. Soc. Am.*, 72, 1185–1194, 1982.

Nakanishi, I., and D. L. Anderson, Measurements of mantle wave velocities and inversion for lateral heterogeneity and anisotropy, 1, Analysis of great circle phase velocities, *J. Geophys. Res.*, 88, 10,267–10,283, 1983.

Nakanishi, I., and D. L. Anderson, Measurements of mantle wave velocities and inversion for lateral heterogeneity and anisotropy, 2, Analysis by the single station method, *Geophys. J. R. Astron. Soc.*, 78, 573–617, 1984.

Nataf, H.-C., and Y. Ricard, 3SMAC: An a priori tomo-

graphic model of the upper mantle based on geophysical modeling, *Phys. Earth Planet. Inter.*, **95**, 101–122, 1996.

Nataf, H.-C., I. Nakanishi, and D. L. Anderson, Measurements of mantle wave velocities and inversion for lateral heterogeneities and anisotropy, 3, Inversion, *J. Geophys. Res.*, **91**, 7261–7307, 1986.

Nelder, J. A. and R. Mead, A simplex method for function minimization, *Comput. J.*, **7**, 308–313, 1965.

Nishimura, C. E., and D. W. Forsyth, Rayleigh wave phase velocities in the Pacific with implications for azimuthal anisotropy and lateral heterogeneities, *Geophys. J. Int.*, **94**, 479–501, 1988.

Nolet, G., S. P. Grand, and B. L. N. Kennett, Seismic heterogeneity in the upper mantle, *J. Geophys. Res.*, **99**, 23,753–23,766, 1994.

Oliver, J., A summary of observed seismic surface wave dispersion, *Bull. Seismol. Soc. Am.*, **52**, 81–86, 1962.

Peterson, J., H. M. Butler, L. G. Holcomb, and C. R. Hutt, The Seismic Research Observatory, *Bull. Seismol. Soc. Am.*, **66**, 2049–2068, 1976.

Press, W. H., B. P. Flannery, S. A. Teukolsky, and W. T. Vetterling, *Numerical Recipes*, Cambridge Univ. Press, New York, 1986.

Ricard, Y., H.-C. Nataf, and J.-P. Montagner, The three-dimensional seismological model a priori constrained: Confrontation with seismic data, *J. Geophys. Res.*, **101**, 8457–8472, 1996.

Snieder, R., Global inversions using normal modes and long-period surface waves, in *Seismic Tomography: Theory and Practice*, edited by H. M. Iyer and K. Hirahara, pp. 23–63, Chapman and Hall, New York, 1993.

Sobel, P. A., and D. H. von Seggern, Applications of surface-wave ray tracing, *Bull. Seismol. Soc. Am.*, **68**, 1359–1380, 1978.

Su, W.-J., R. L. Woodward, and A. M. Dziewonski, Deep origin of mid-ocean-ridge seismic velocity anomalies, *Nature*, **359**, 149–152, 1992.

Su, W.-J., R. L. Woodward, and A. M. Dziewonski, Degree 12 model of shear velocity heterogeneity in the mantle, *J. Geophys. Res.*, **99**, 6945–6980, 1994.

Tams, E., Über die Fortpflanzungsgeschwindigkeit der seismischen Oberflächenwellen längs kontinentaler und ozeanischer Wege, *Centralbl. Mineral. Geol. Paläontol.*, no. 2, 44–52, 1921a.

Tams, E., Über die Fortpflanzungsgeschwindigkeit der seismischen Oberflächenwellen längs kontinentaler und ozeanischer Wege, *Centralbl. Mineral. Geol. Paläontol.*, no. 3., 75–83, 1921b.

Tanimoto, T., The Backus-Gilbert approach to the 3-D structure in the upper mantle, I, Lateral variation of surface wave phase velocity with its error and resolution, *Geophys. J. R. Astron. Soc.*, **82**, 105–123, 1986.

Tanimoto, T., and D. L. Anderson, Lateral heterogeneity and azimuthal anisotropy of the upper mantle: Love and Rayleigh waves 100–250 s, *J. Geophys. Res.*, **90**, 1842–1858, 1985.

Toksöz, M. N., and D. L. Anderson, Phase velocities of long-period surface waves and structure of the upper mantle, 1, Great circle Love and Rayleigh wave data, *J. Geophys. Res.*, **71**, 1649–1658, 1966.

Trampert, J., and J. H. Woodhouse, Global phase velocity maps of Love and Rayleigh waves between 40 and 150 seconds, *Geophys. J. Int.*, **122**, 675–690, 1995.

Trampert, J., and J. H. Woodhouse, High resolution global phase velocity distributions, *Geophys. Res. Lett.*, **23**, 21–24, 1996.

Tromp, J., and F. A. Dahlen, Variational principles for surface wave propagation on a laterally heterogeneous Earth, II, Frequency-domain JWKB theory, *Geophys. J. Int.*, **109**, 599–619, 1992.

Tromp, J., and F. A. Dahlen, Maslov theory for surface wave propagation on a laterally heterogeneous Earth, *Geophys. J. Int.*, **115**, 512–528, 1993.

Wong, Y. K., Upper mantle heterogeneity from phase and amplitude data of mantle waves, Ph.D. thesis, Harvard Univ., Cambridge, Mass., 1989.

Woodhouse, J. H., and A. M. Dziewonski, Mapping the upper mantle: Three-dimensional modeling of Earth structure by inversion of seismic waveforms, *J. Geophys. Res.*, **89**, 5953–5986, 1984.

Woodhouse, J. H., and Y. K. Wong, Amplitude, phase and path anomalies of mantle waves, *Geophys. J. R. Astron. Soc.*, **87**, 753–773, 1986.

Wu, F. T., Mantle Rayleigh wave dispersion and tectonic provinces, *J. Geophys. Res.*, **77**, 6445–6453, 1972.

Zhang, Y.-S., and T. Lay, Global surface wave phase velocity variations, *J. Geophys. Res.*, **101**, 8415–8436, 1996.

Zhang, Y.-S., and T. Tanimoto, Ridges, hotspots and their interaction as observed in seismic velocity maps, *Nature*, **355**, 45–49, 1992.

---

G. Ekström, E. W. F. Larson, J. Tromp, Department of Earth and Planetary Sciences, Hoffman Laboratory, Harvard University, 20 Oxford Street, Cambridge MA 02138. (e-mail: ekstrom@eps.harvard.edu; larson@eps.harvard.edu; tromp@eps.harvard.edu)

June 24, 1996; revised November 26, 1996; accepted December 2, 1996.

**Figure 1.** The six B-spline basis functions  $f_i$  used to parameterize the apparent phase velocity perturbation  $\bar{\delta}c$  and the spectral amplitude  $A$ .

**Figure 2.** Eleven partially overlapping frequency bands, evenly spaced in frequency between 250 and 32 s period.

**Figure 3.** Comparison of observed and model seismograms at progressive stages of the inversion. (a) Initial fit, before adjustment of phase velocity and amplitude, 250–32 s. (b) Initial fit, 250–75 s. While the misfit is large, it is apparent that the waveform can be matched after minor adjustments of the phase. (c) Fit after adjustment of  $\bar{\delta}c(\omega)$  and  $A(\omega)$  in the period band 250–75 s. (d) Fit after adjustment in the period band 250–40 s. (e) Final result after fitting the data in the period band 250–32 s.

**Figure 4.** Dispersion and spectral amplitude results for the analysis summarized in Figure 3. (a) Initial guess (from SH8U4L8) and final result for the phase velocity perturbation expressed as a percentage of the preliminary reference Earth model (PREM) phase velocity at each frequency. (b) Initial and final amplitude spectra, normalized to the largest value in the range of frequencies.

**Figure 5.** Map showing the locations of 1744 earthquakes (hexagons) and 158 stations (squares), each of which forms the start or end point for at least one successfully measured Love or Rayleigh wave path.

**Figure 6.** Distribution of phase measurement differences for Rayleigh waves at 75 s and pairwise similar paths. The three different curves correspond to measurements of A, B, and C quality. The curves have been normalized to have the same area.

**Figure 7.** Dispersion, expressed as perturbations with respect to PREM, determined for the six tectonic regions of GTR1 [Jordan, 1981]. (a) Love waves. (b) Rayleigh waves.

**Figure 8.** Variance reduction of the complete data set and three global models: the GTR1 regionalization and dispersion curves, the  $L = 16$  undamped spherical harmonic model, and the preferred  $L = 40$  smooth model. (a) Love waves. (b) Rayleigh waves.

**Figure 9.** The goodness of fit parameter  $\chi^2/N$  calculated for different inversions and models: the GTR1 regionalization and dispersion curves, the  $L = 16$  undamped spherical harmonic model, and the preferred  $L = 40$  smooth model. (a) Love waves. (b) Rayleigh waves.

**Figure 10.** The rms value of the velocity perturbations at different periods for the undamped  $L = 16$  inversions. The  $l = 0$  term is not included in the rms value.

**Figure 11.** Trade-off curve for the  $L = 40$  inversion of Love waves at 60 s period, showing the effect of choosing different values of  $\gamma$  in equation (25). The shape of the curve is representative of all  $L = 40$  inversions.

**Figure 12.** (top) The Love wave phase velocity at 35 s predicted from Mooney *et al.*'s [1995] model of the crust. (bottom) The recovery of this model after synthesizing observations corresponding to the actual path coverage, adding realistic noise, and performing the damped inversion.

**Figure 13.** Graph showing the recovery of individual spherical harmonic degrees in the resolution test. (a) Power of individual degrees in the model. Solid triangles correspond to the input model; open ones correspond to the retrieved model. (b) Correlation between the input and retrieved models as a function of angular degree.

**Figure 14.** The spherical average phase velocity perturbation with respect to PREM for Love and Rayleigh waves.

**Figure 15.** (a) Correlation between our preferred  $L = 40$  maps and the phase velocity maps calculated from the crustal model of Mooney *et al.* [1995]. Both the global value and the value for continental areas alone are shown. (b) The observed rms value of Love wave phase velocity variations compared with the predictions from Mooney *et al.*'s [1995] crustal model. The rms value of the difference between observed and predicted phase velocity variations is also shown. (c) Same as (b), except for Rayleigh waves.

**Figure 16.** Comparison of *Trampert and Woodhouse's* [1996] Love wave map at 40 s and ours. (a) Correlation of individual spherical harmonic degrees. (b) Power of the two models at degrees 1–40.

**Figure 17.** Regional map showing the Love wave phase velocity at 40 s period. (top) The map of *Trampert and Woodhouse* [1996] and (bottom) our results. In general, there is less correlation in the top map with known crustal and tectonic structures, such as the thick crust of Tibetan platform and the continent–ocean contrast around India. In other areas, for example, east of 100°E, the two models are extremely similar. The overall correlation between the two regional maps is 0.68.

**Plate 1a.** Global Love wave phase velocity maps at 35, 50, 75, and 150 s. Note that the color scale is different for each map.

**Plate 1b.** Global Rayleigh wave phase velocity maps at 35, 50, 75, and 150 s. Note that the color scale is different for each map.

**Table 1.** Number of Observations

Period	<i>N</i> (Love)	<i>N</i> (Rayleigh)
35	15,473	28,457
37	15,473	28,457
40	15,721	28,663
45	15,780	28,779
50	22,633	37,104
60	23,193	37,734
75	23,228	37,739
100	22,498	37,374
150	16,798	33,475

**Table 2.** Empirically Determined Observational Uncertainties

Period	Love Waves			Rayleigh Waves		
	$\sigma_A$	$\sigma_B$	$\sigma_C$	$\sigma_A$	$\sigma_B$	$\sigma_C$
35	0.812	1.164	2.490	1.300	2.056	3.519
37	0.727	0.943	1.805	1.169	1.753	2.653
40	0.644	0.797	1.295	1.045	1.553	2.057
45	0.550	0.644	0.922	0.821	1.290	1.599
50	0.507	0.709	1.103	0.822	1.391	2.016
60	0.388	0.511	0.682	0.645	1.042	1.390
75	0.308	0.399	0.494	0.444	0.651	0.832
100	0.243	0.330	0.410	0.322	0.449	0.547
150	0.194	0.253	0.290	0.220	0.294	0.310

**Table 3.** Results and Comparisons With Other Models

Period	$L = 16^a$		$L = 40^b$		TW95 <sup>c</sup>		TW96 <sup>d</sup>		M et al. <sup>e</sup>		LM <sup>f</sup>		ZL <sup>g</sup>	
	$\frac{\delta c_{rms}}{c_0}$	$\mathcal{R}$												
L 35	4.00	46.2	3.91	78.5					4.48	91.0				
L 37	3.69	46.7	3.62	82.5					4.16	89.9				
L 40	3.29	47.5	3.25	86.9	2.79	105.0	2.94	154.2	3.75	88.4				
L 45	2.83	52.9	2.77	91.3					3.21	86.6				
L 50	2.42	54.3	2.42	101.3					2.82	85.3				
L 60	2.02	61.7	2.02	109.1	2.06	117.8	2.05	188.8	2.29	83.7				
L 75	1.80	70.4	1.77	113.0					1.84	82.2	1.57	60.1		
L 100	1.63	74.9	1.56	102.9	1.69	85.0	1.72	251.6	1.45	80.6	1.41	54.1	1.60	65.6
L 150	1.40	72.4	1.27	71.7	1.71	73.9	1.44	163.3	1.08	78.7	1.25	52.1	1.47	55.4
R 35	2.49	54.4	2.46	90.0					2.00	114.8				
R 37	2.32	56.5	2.30	92.2					1.84	116.8				
R 40	2.14	59.4	2.13	93.4	2.12	127.7	2.08	179.6	1.66	118.7				
R 45	1.99	62.4	1.99	100.2					1.44	119.5				
R 50	1.90	62.1	1.91	101.9					1.30	118.3				
R 60	1.82	61.7	1.82	101.3	1.98	136.9	2.04	200.4	1.13	113.2				
R 75	1.66	61.9	1.69	107.4					1.00	104.8	1.43	54.3		
R 100	1.38	64.1	1.38	103.4	1.33	98.1	1.68	247.3	0.88	94.3	1.18	48.4	1.22	77.2
R 150	0.93	66.6	0.87	84.3	0.99	115.8	1.10	164.0	0.72	83.5	0.92	56.4	0.90	72.7

<sup>a</sup>Undamped inversion with  $L = 16$  (this study).<sup>b</sup>Damped inversion with  $L = 40$  (this study).<sup>c</sup>Trampert and Woodhouse [1995].<sup>d</sup>Trampert and Woodhouse [1996].<sup>e</sup>Phase velocity maps calculated from Mooney et al. [1995].<sup>f</sup>Laske and Masters [1996].<sup>g</sup>Zhang and Lay [1996].

**Table 4.** Correlations of  $L = 40$  Results With Other Models

Period	$L = 16^a$ 16 <sup>g</sup>	TW95 <sup>b</sup> 40 <sup>g</sup>	TW96 <sup>c</sup> 40 <sup>g</sup>	M et al. <sup>d</sup> 40 <sup>g</sup>	LM <sup>e</sup> 24 <sup>g</sup>	ZL <sup>f</sup> 30 <sup>g</sup>
L 35	0.97			0.83		
L 40	0.97	0.82	0.80	0.79		
L 60	0.97	0.82	0.78	0.49		
I 75	0.97			0.28	0.83	
L 100	0.97	0.83	0.65	0.09	0.81	0.82
L 150	0.95	0.81	0.67	-0.09	0.85	0.82
R 35	0.98			0.54		
R 40	0.98	0.84	0.81	0.36		
R 60	0.98	0.84	0.79	-0.10		
R 75	0.98			-0.22	0.81	
R 100	0.99	0.80	0.68	-0.28	0.81	0.69 <sup>h</sup>
R 150	0.98	0.64	0.62	-0.23	0.77	0.62 <sup>i</sup>

<sup>a</sup>Undamped inversion with  $L = 16$  (this study).<sup>b</sup>Trampert and Woodhouse [1995].<sup>c</sup>Trampert and Woodhouse [1996].<sup>d</sup>Phase velocity maps calculated from Mooney et al. [1995].<sup>e</sup>Laske and Masters [1996].<sup>f</sup>Zhang and Lay [1996].<sup>g</sup>Highest degree ( $L_{\max}$ ) in model.<sup>h</sup> $L_{\max} = 28$ .<sup>i</sup> $L_{\max} = 24$ .

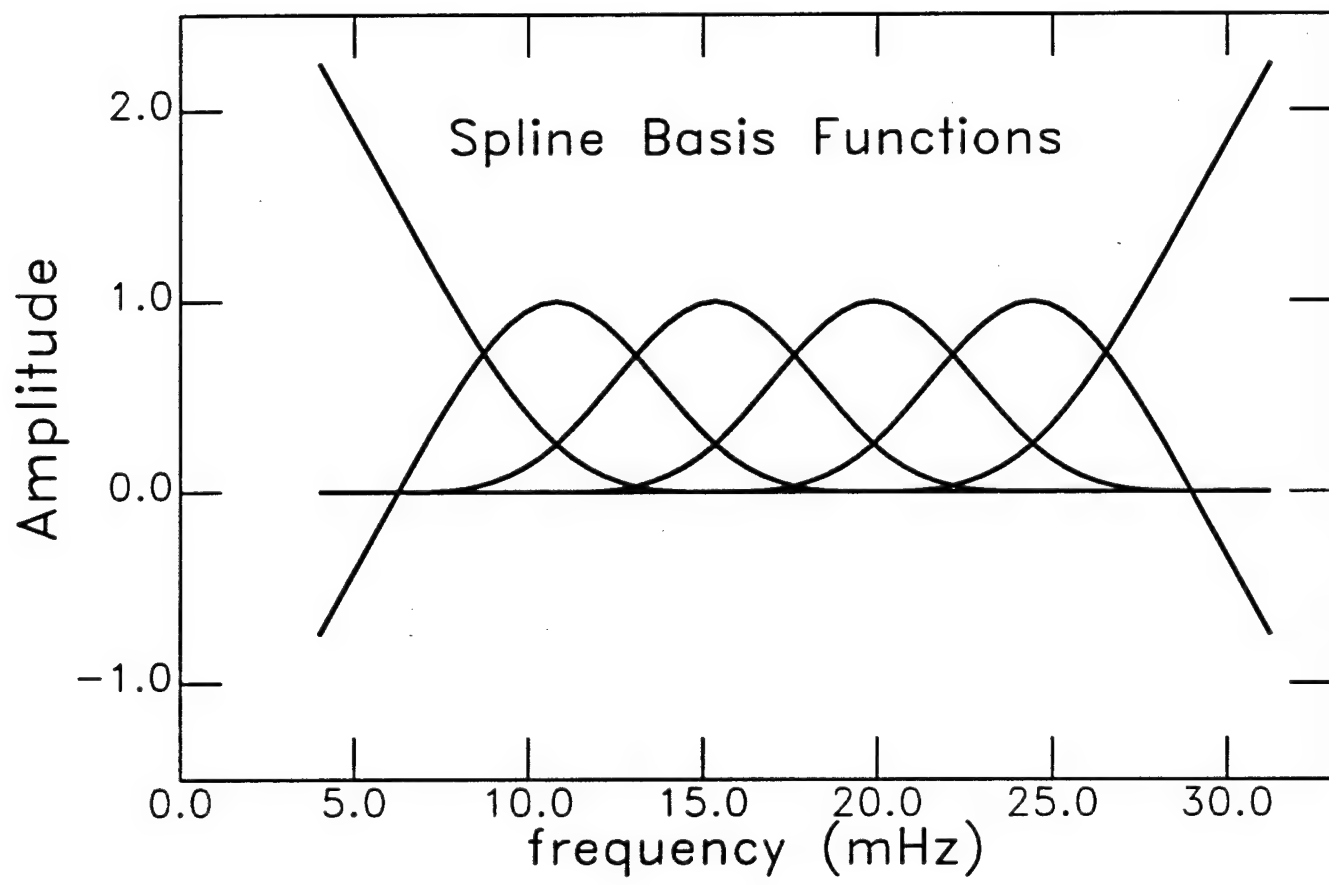


**Figure 1**

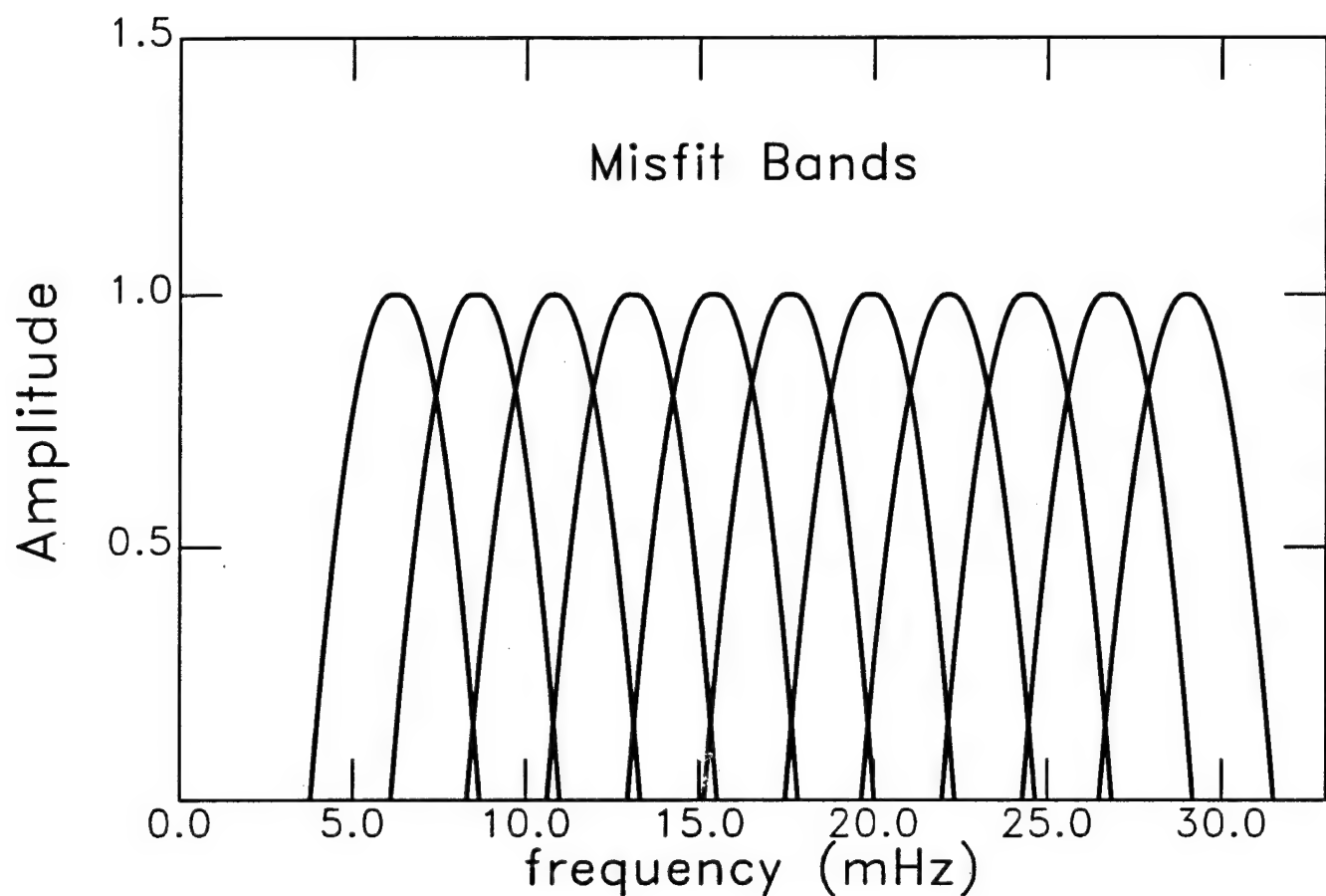


**Figure 2**

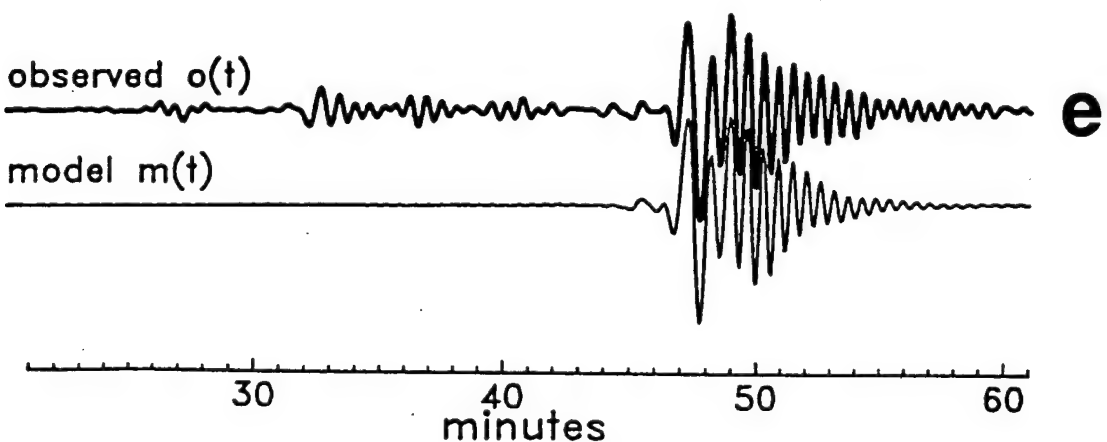
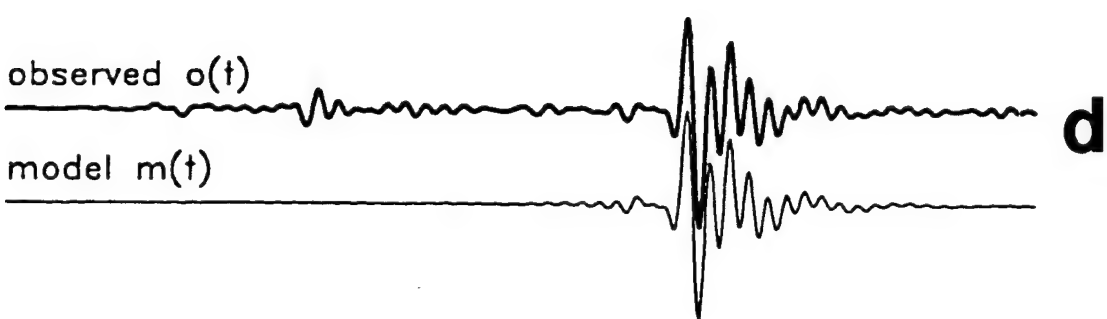
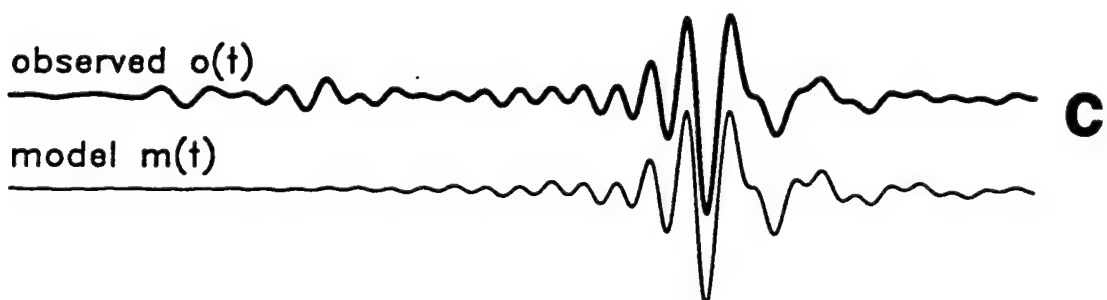
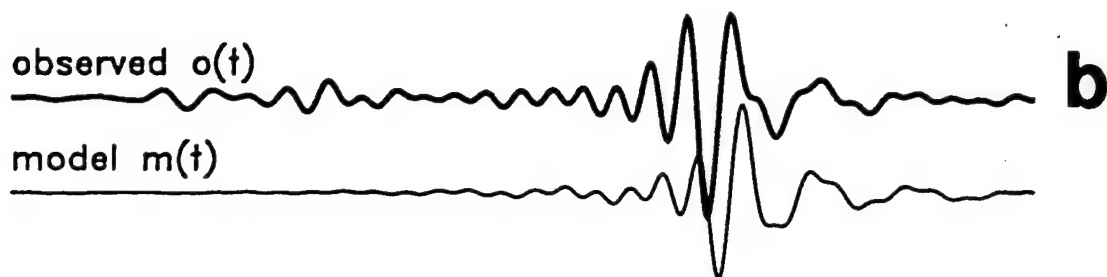
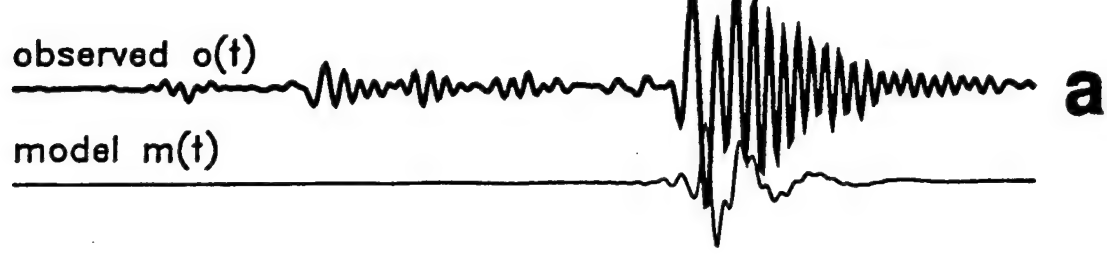


**Fig. 3**

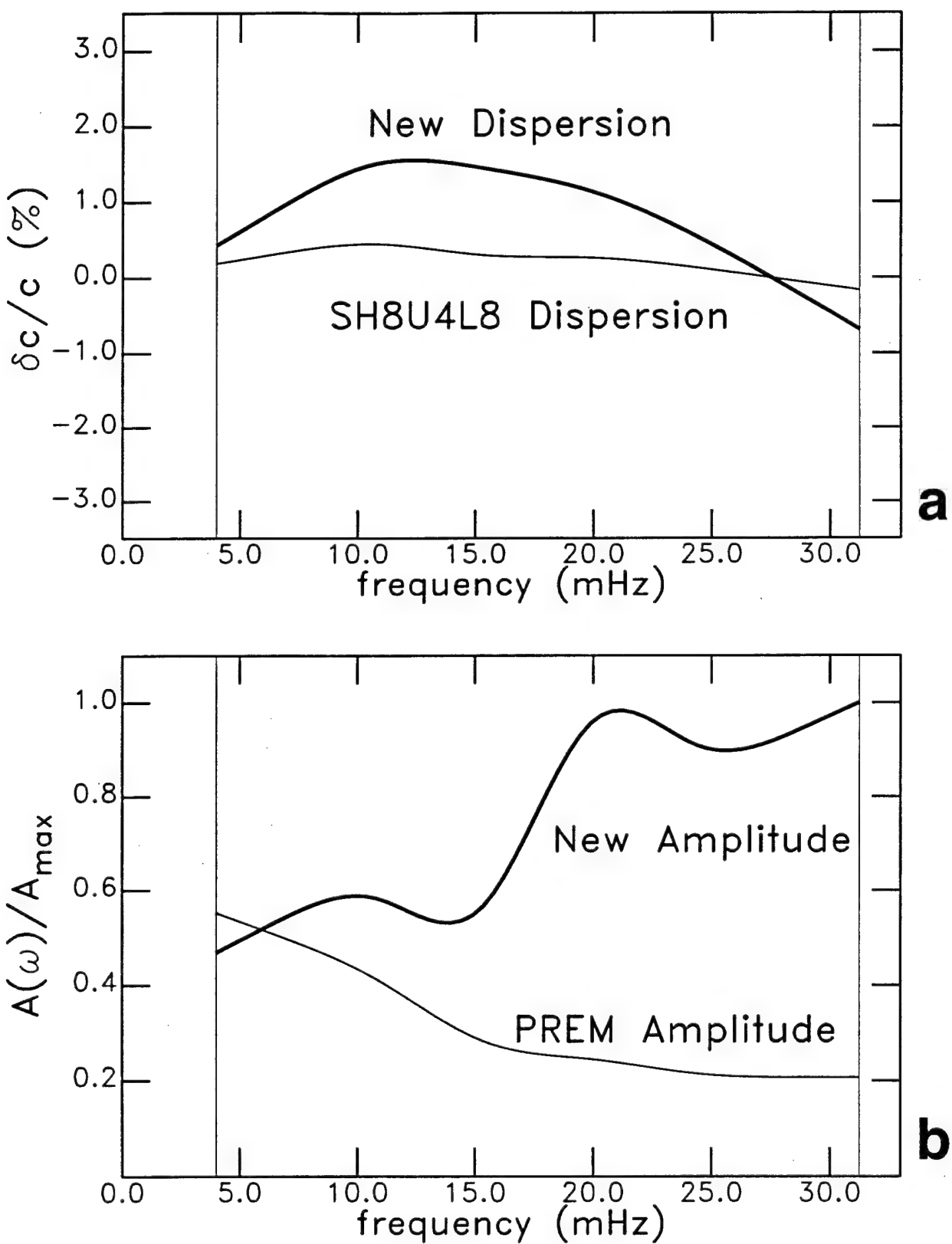
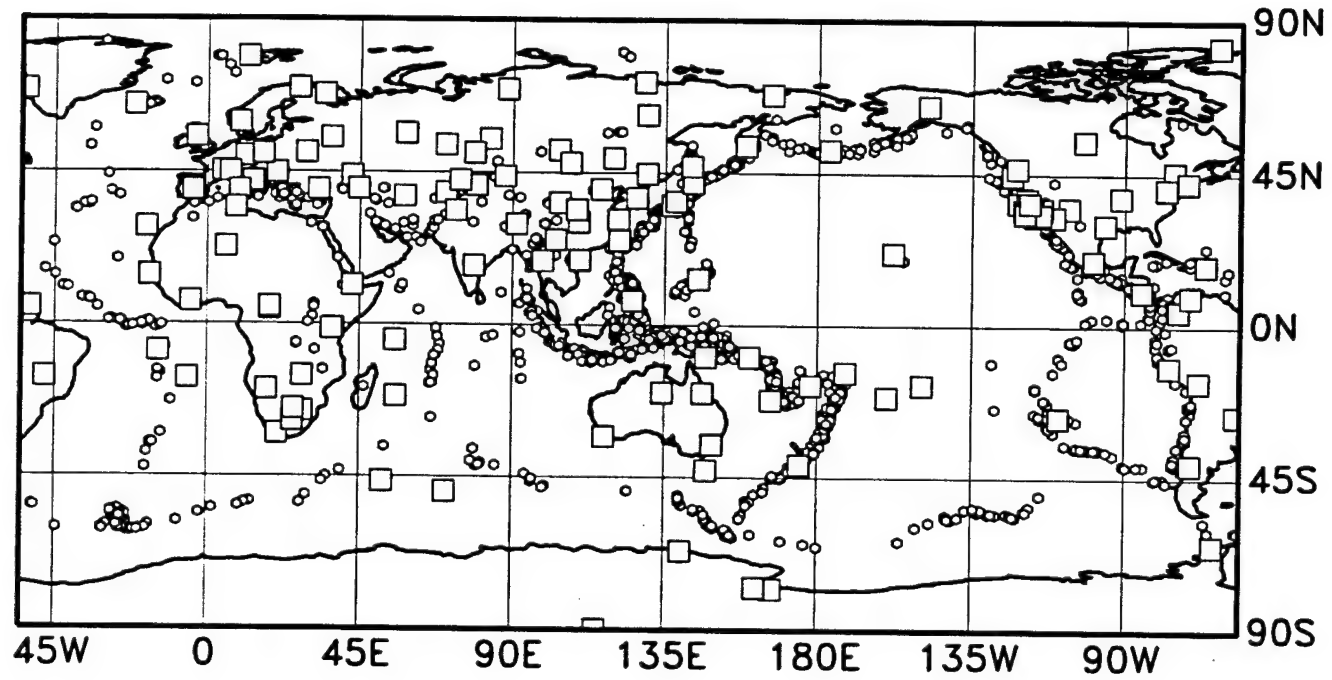
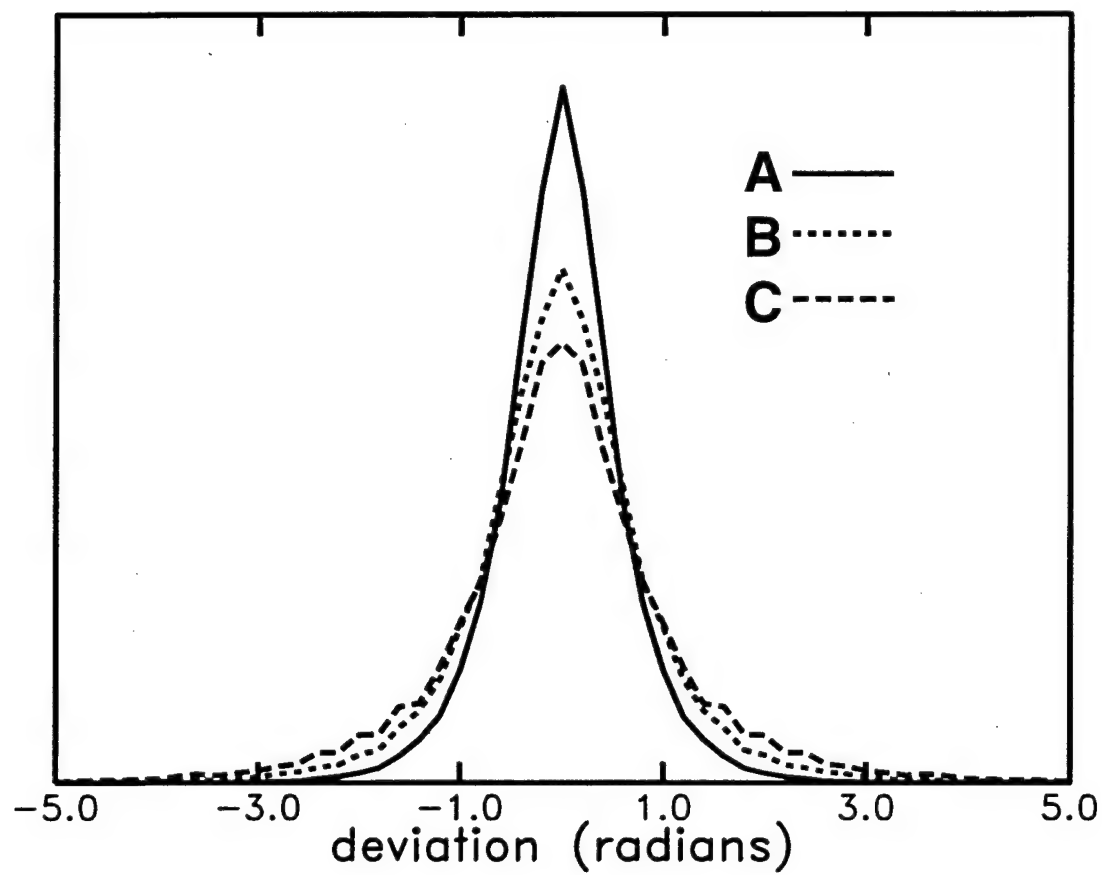


Figure 4



**Figure 5**



**Figure 6**

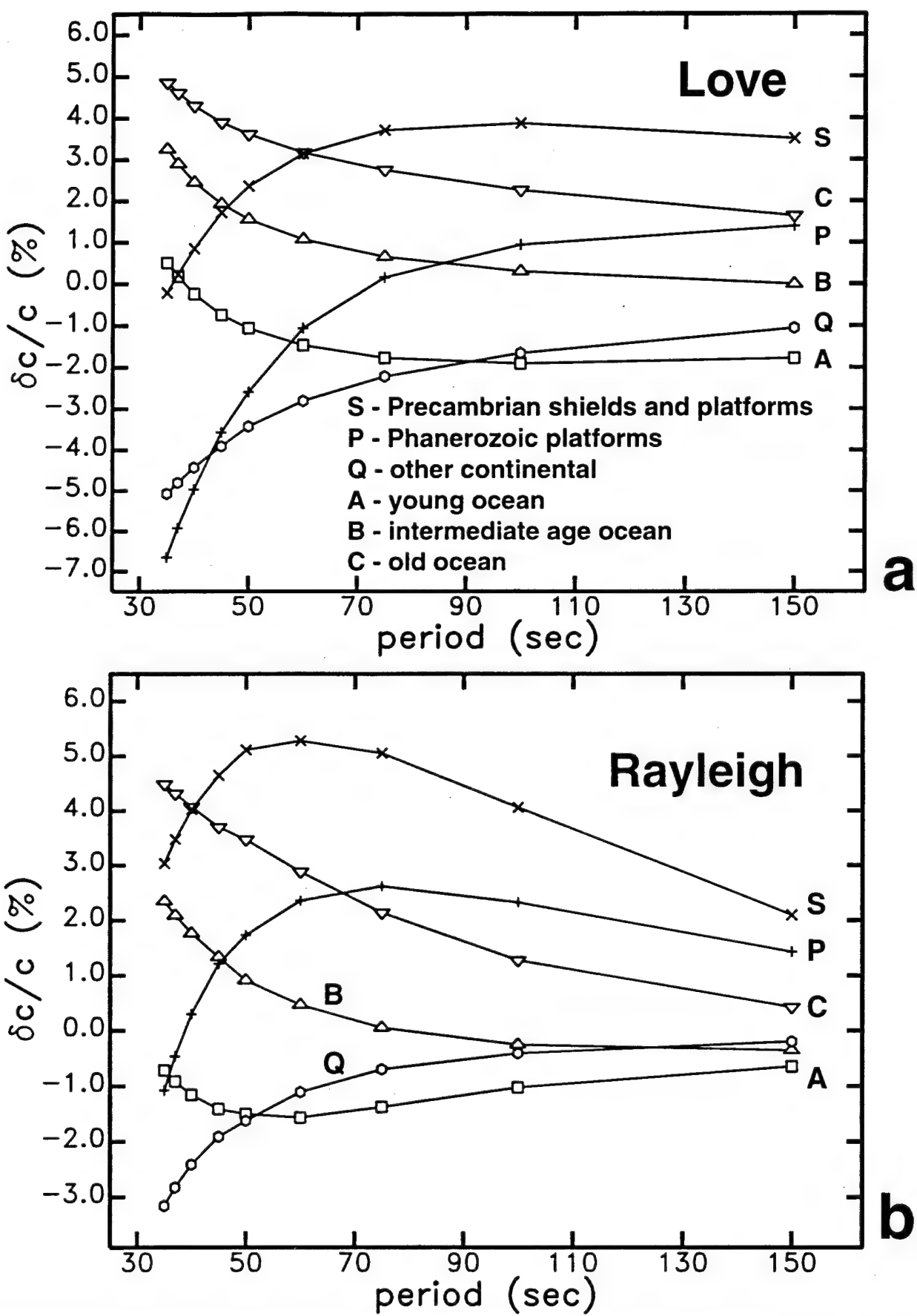


Figure 7

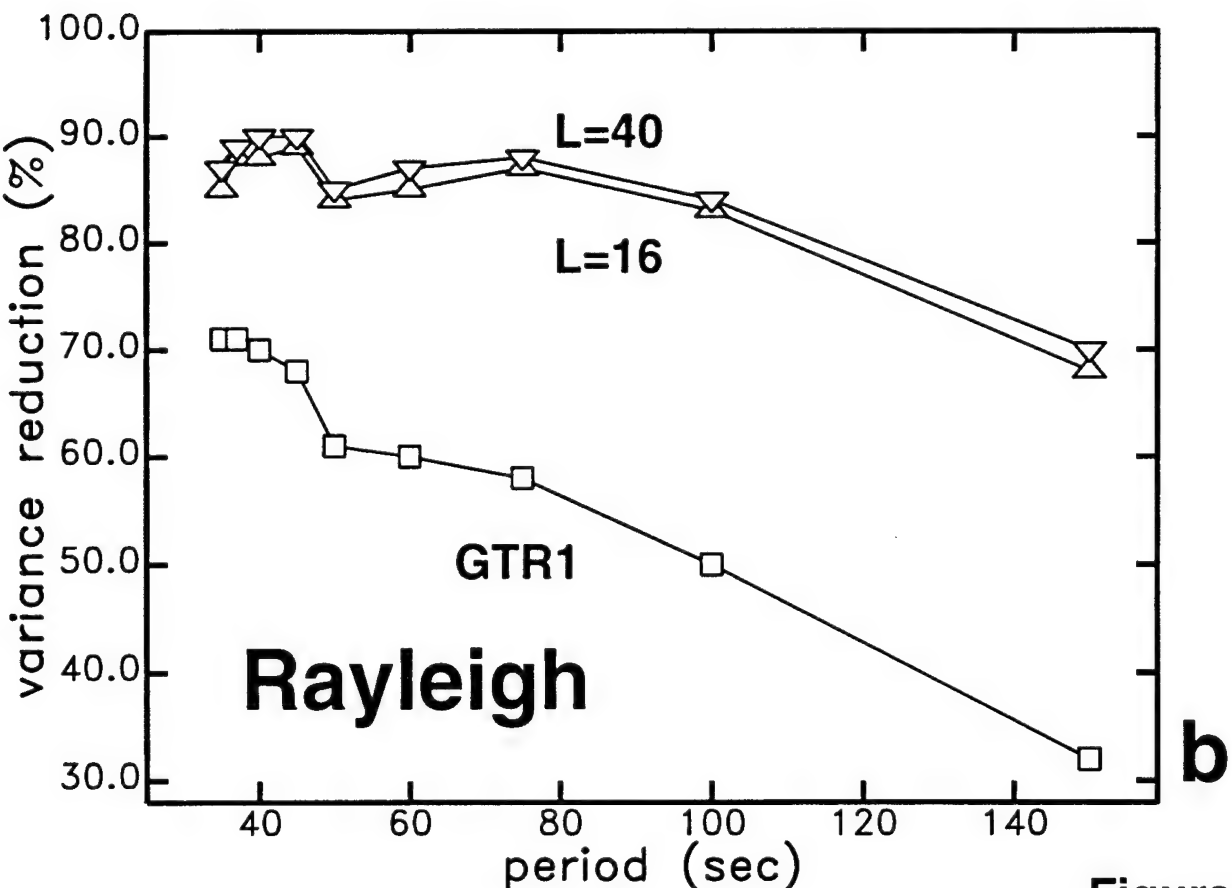
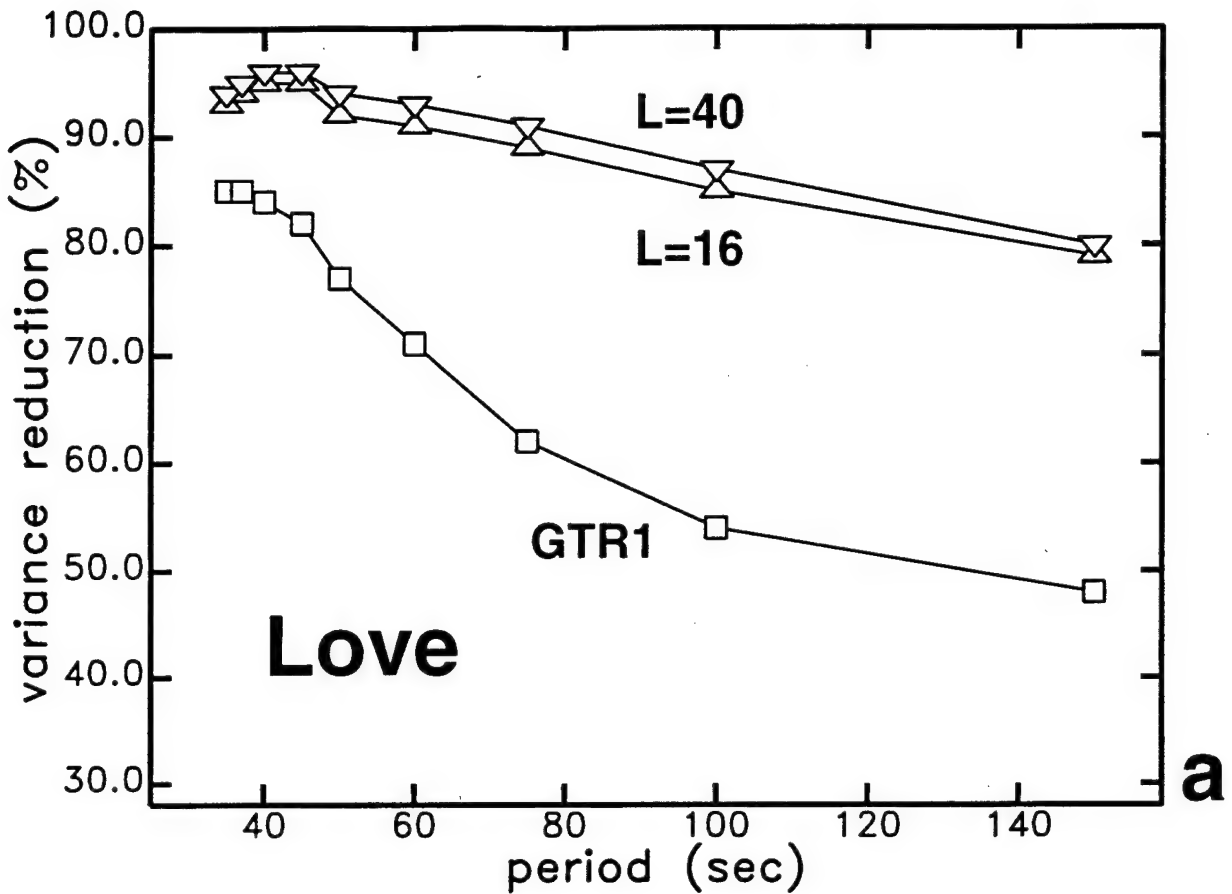


Figure 8

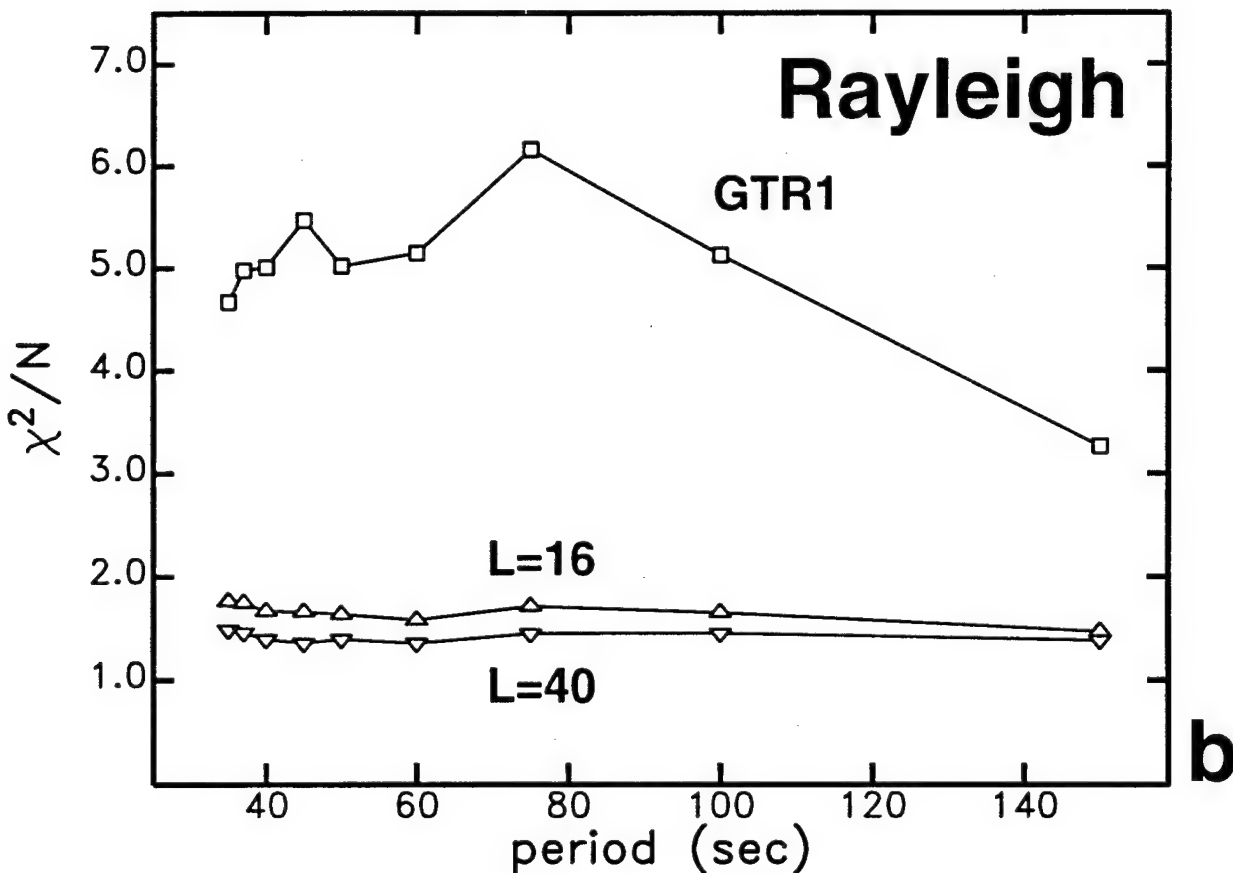
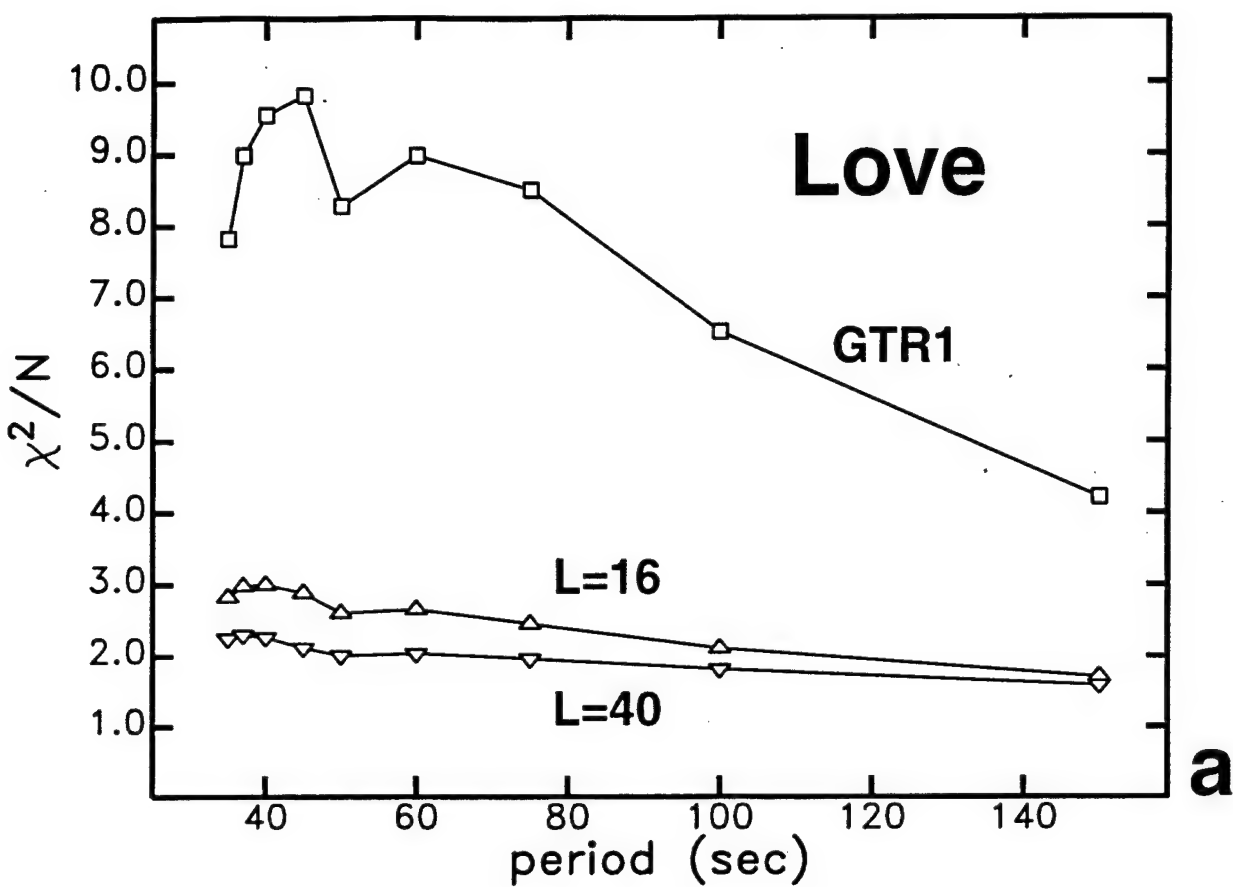
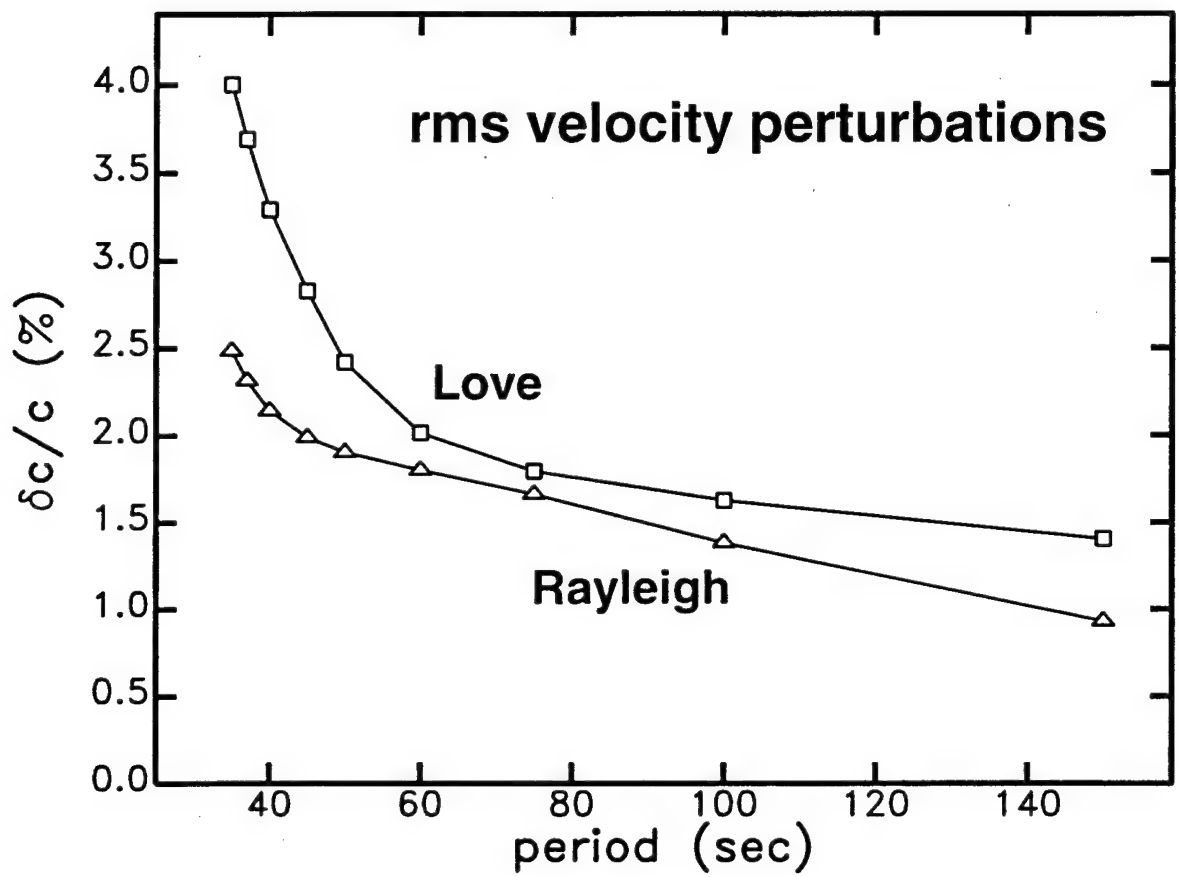


Figure 9



**Figure 10**

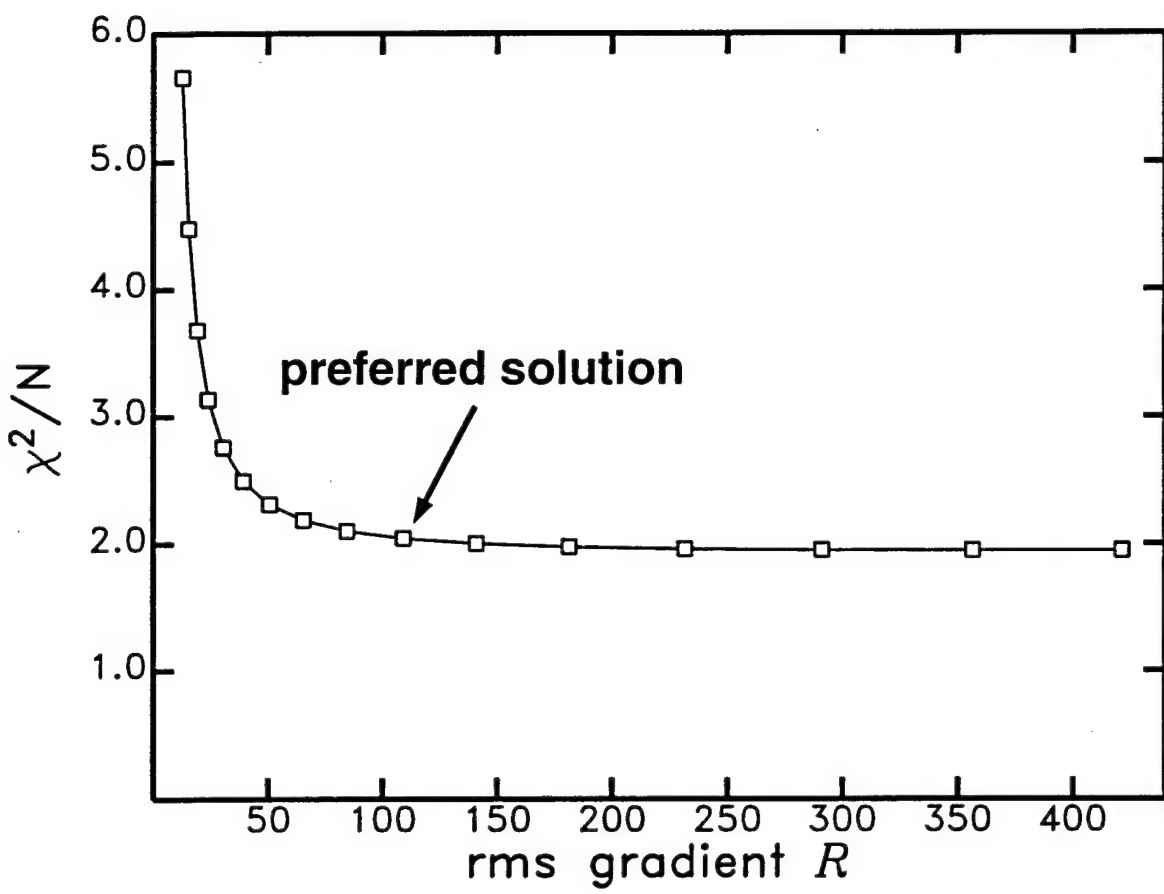
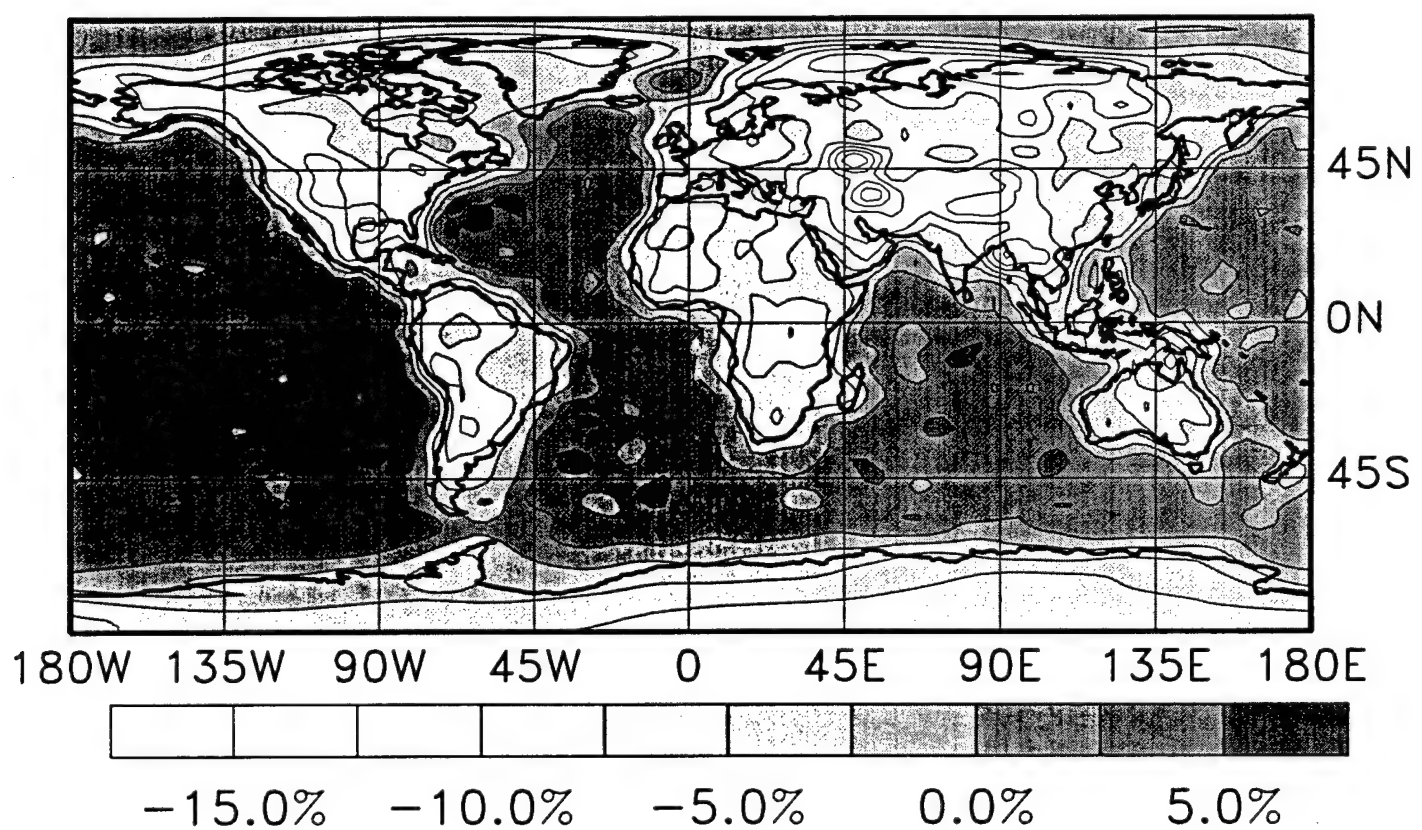
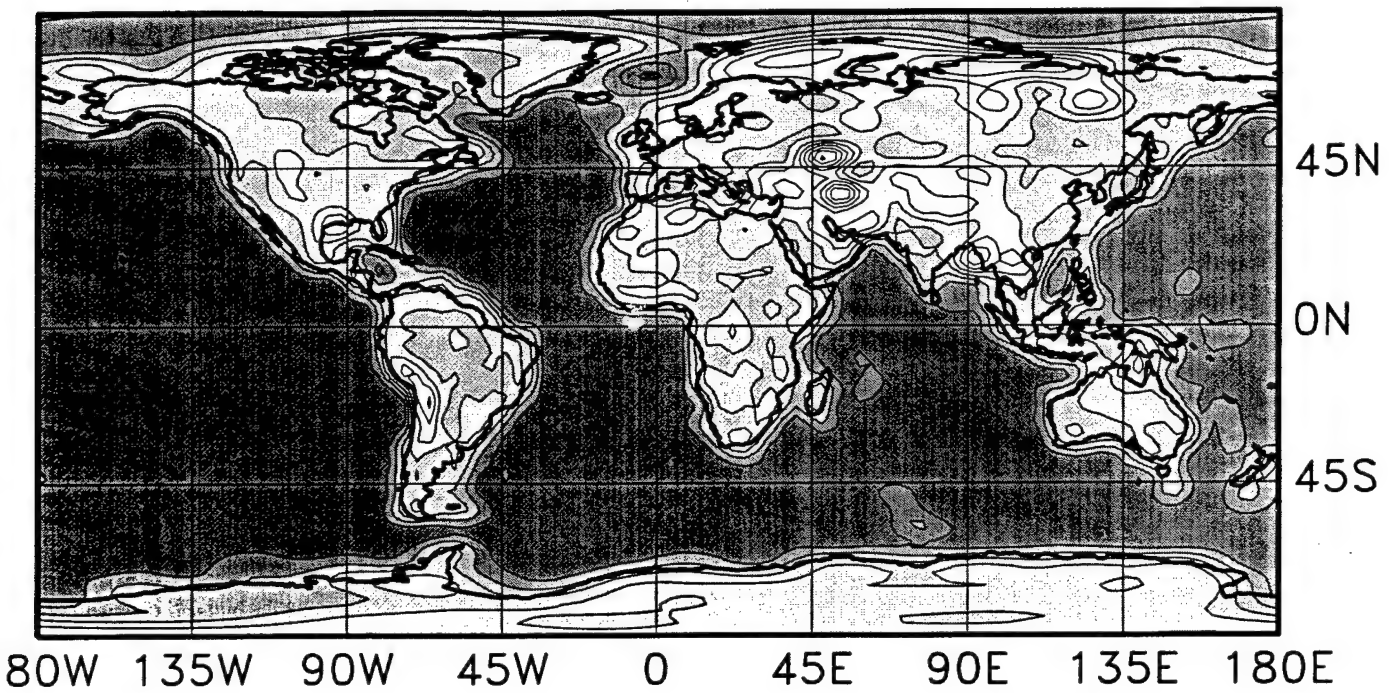
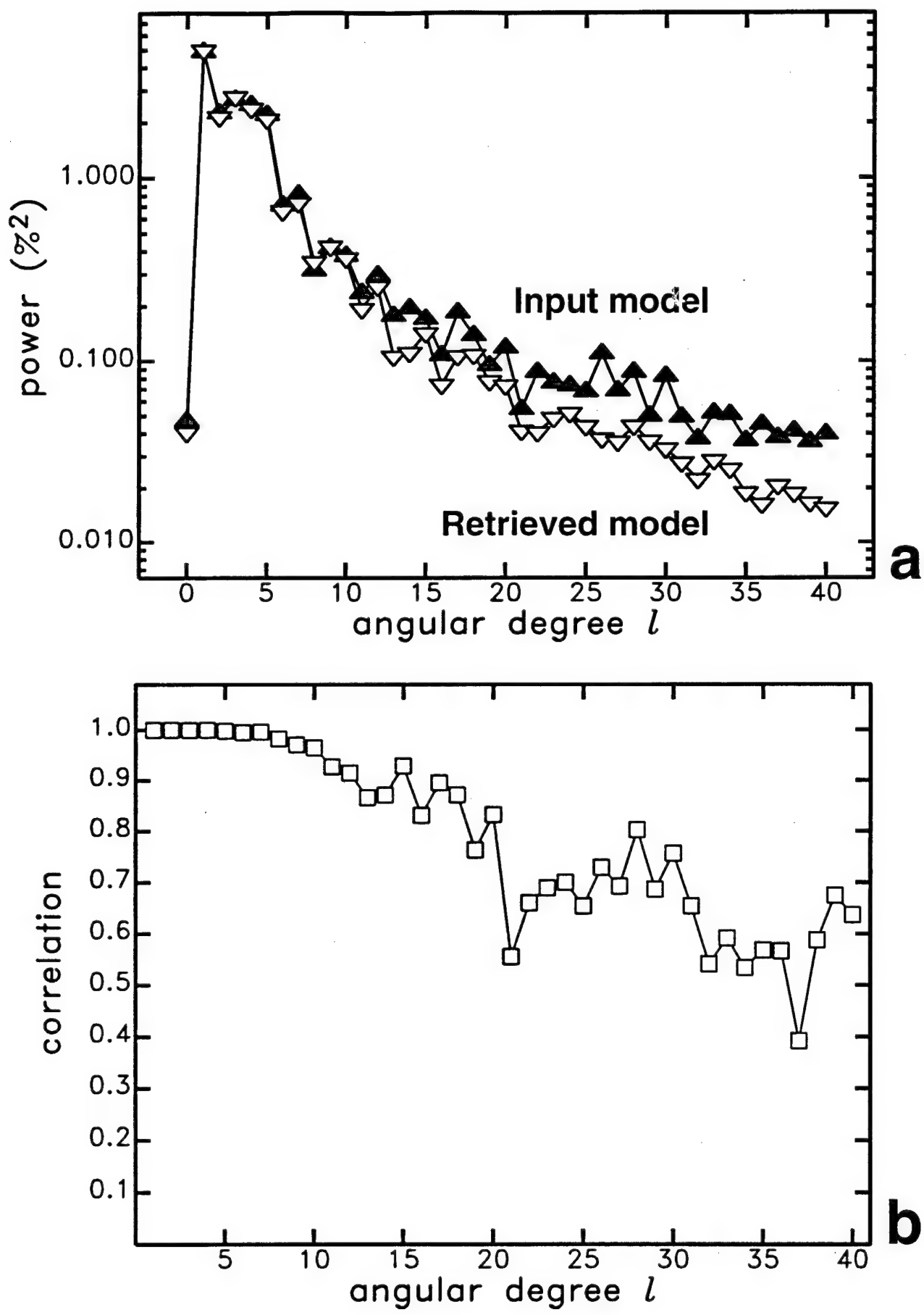


Figure 11



**Figure 12**



**Figure 13**

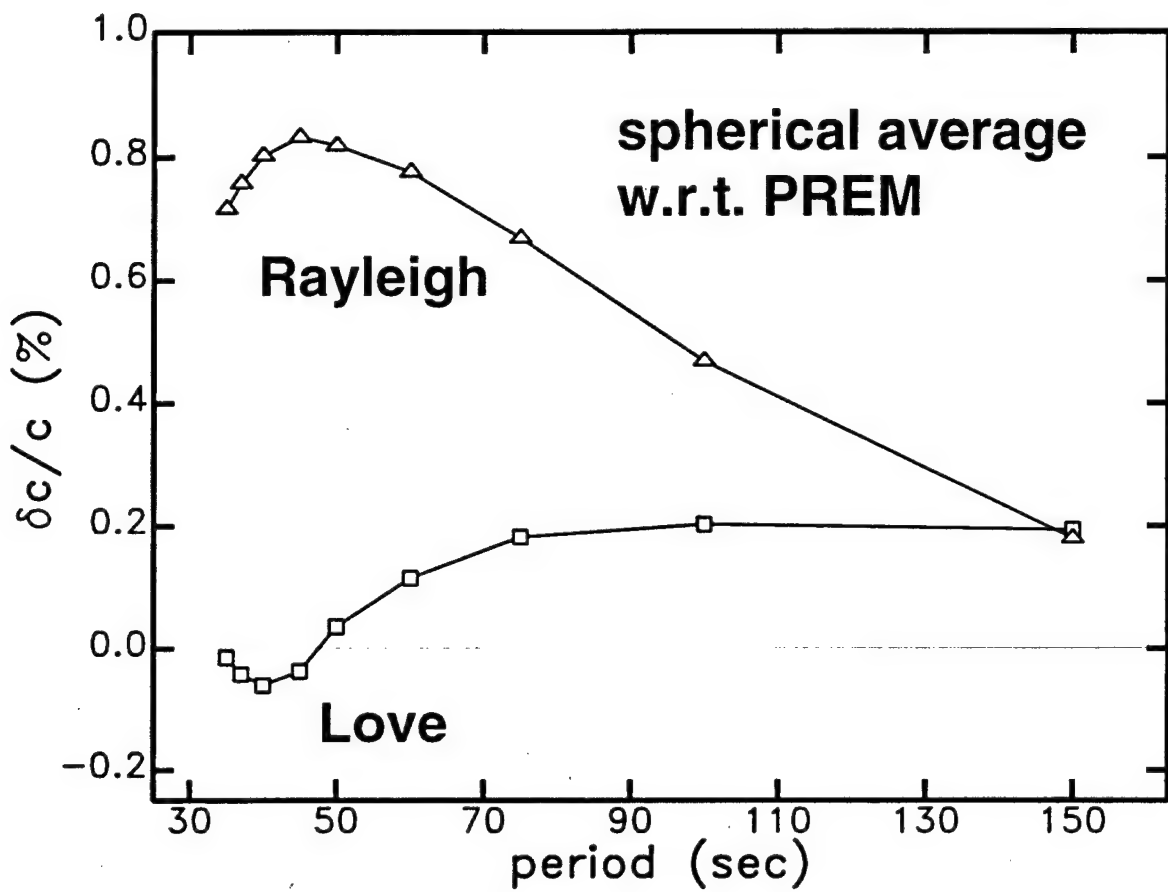
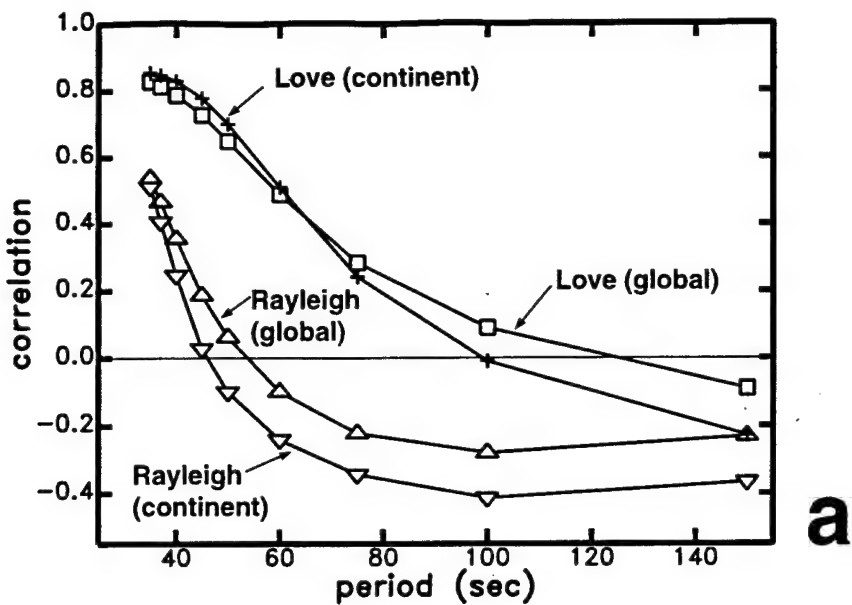
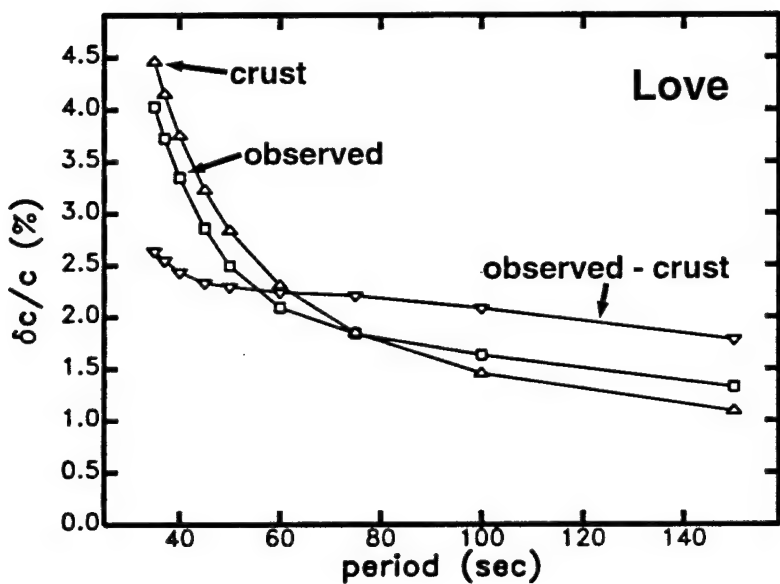


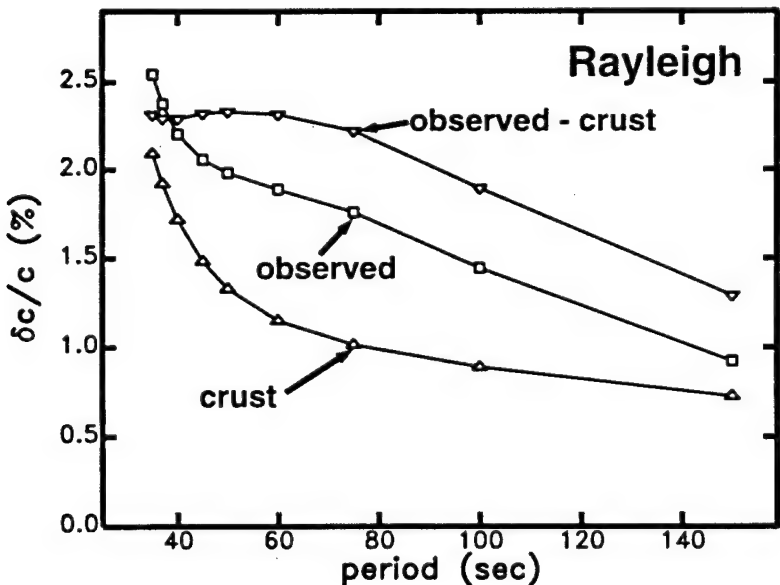
**Figure 14**



a



b



c

Figure 15

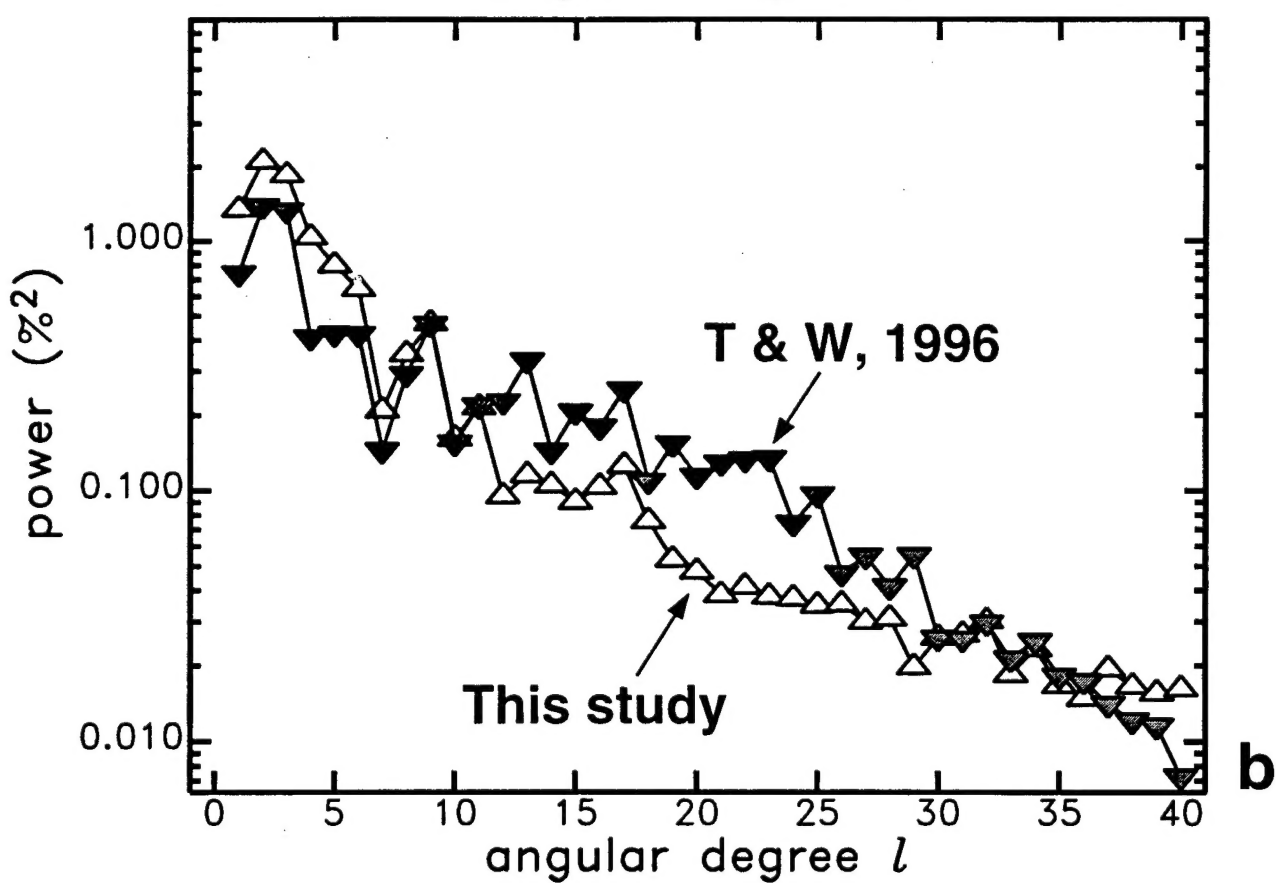
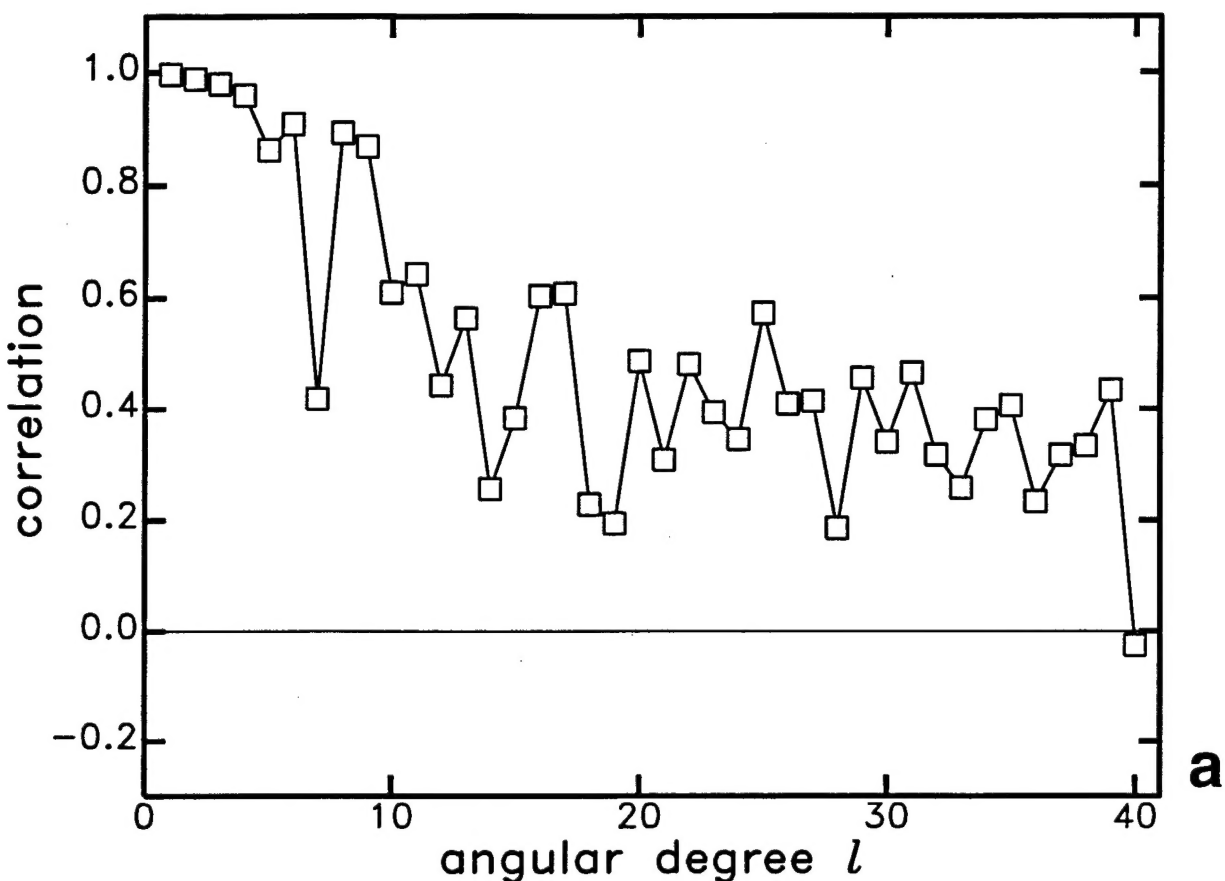
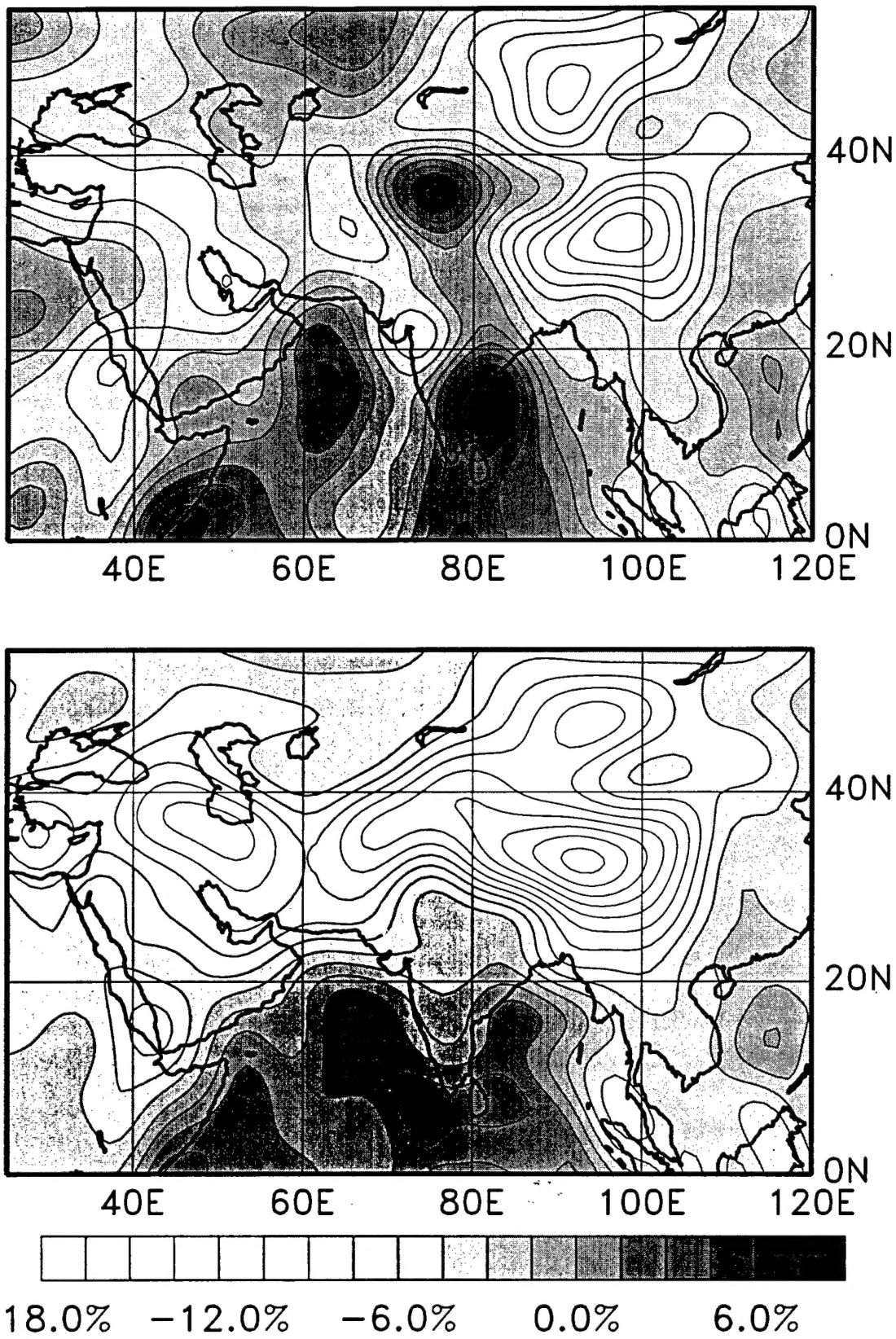


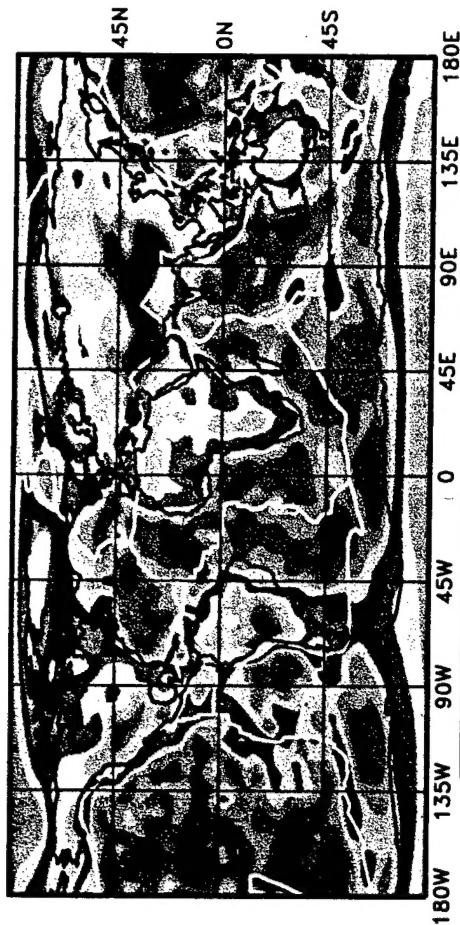
Figure 16



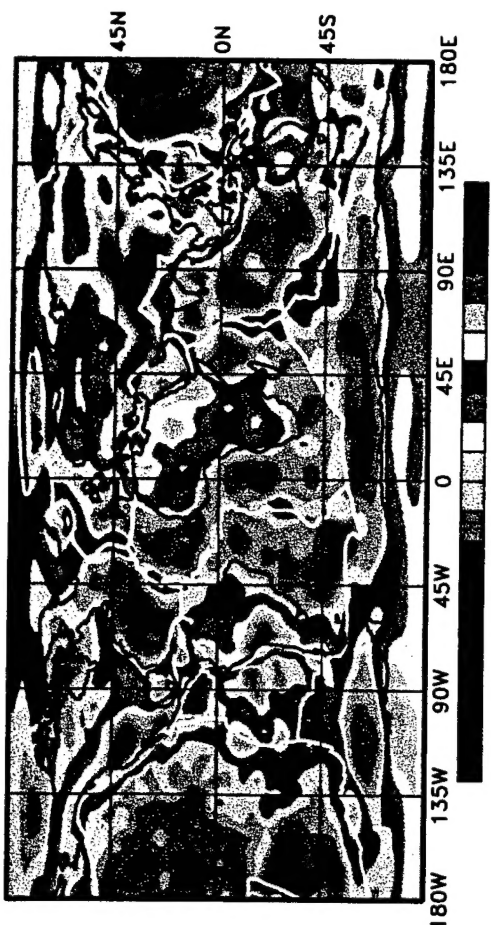
**Figure 17**

# Love

35 S



50 S



75 S

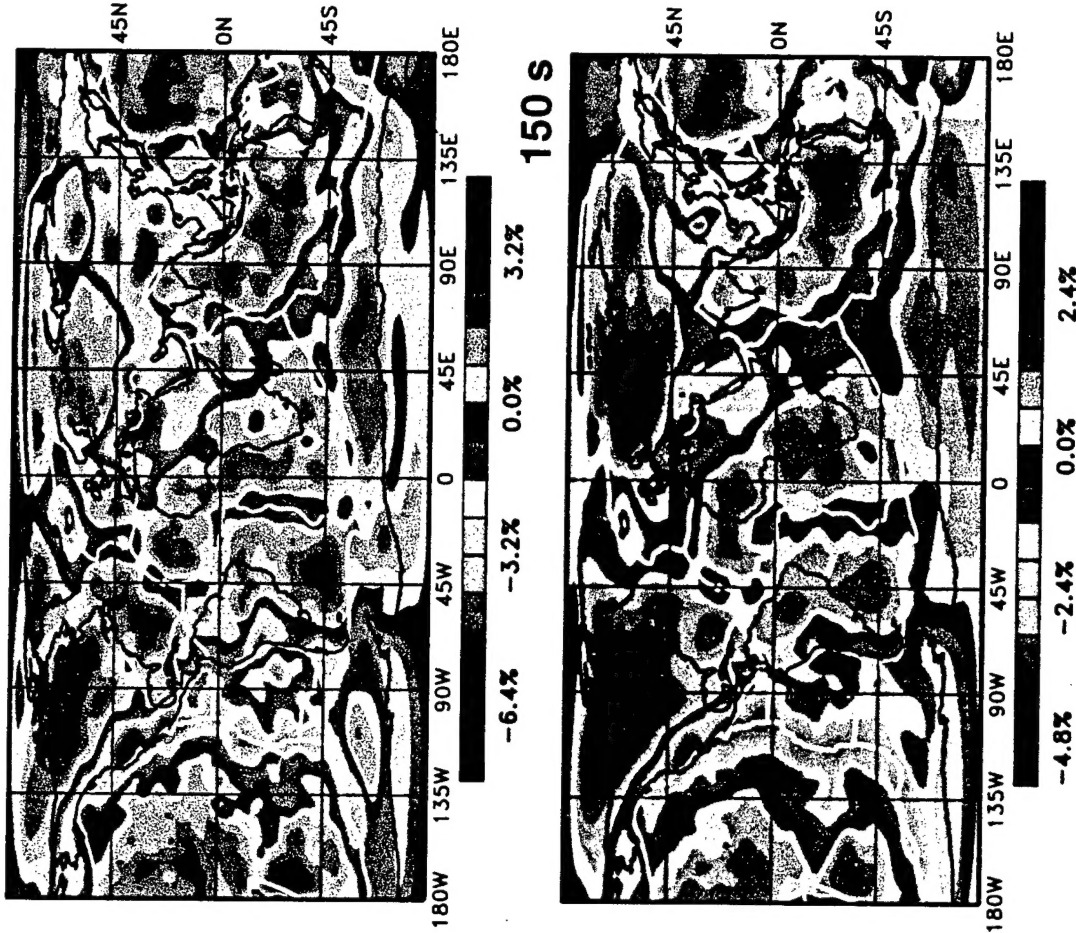
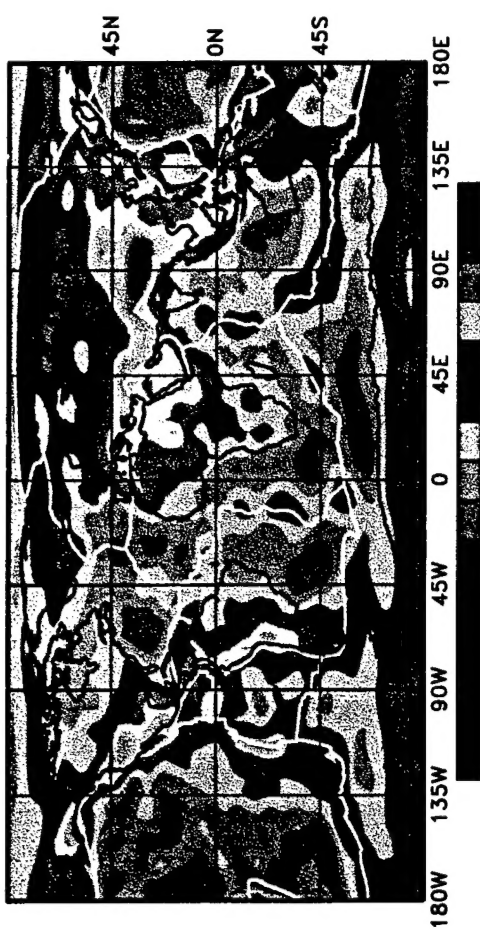


Plate 1a

# Rayleigh

35 S



75 S

